Electrostatics of Particle Confinement within Nanochannels: Role of Double-Layer Interactions and Ion-Ion Correlations

Inderbir S. Sidhu* and Amalie L. Frischknecht+ and Paul J. Atzberger**
+Technical Staff, Center for Integrated Nanotechnologies, Sandia National Laboratories.
*Undergraduate Researcher, Department of Mathematics, University of California Santa Barbara.
**Professor, Department of Mathematics, University of California Santa Barbara,
e-mail: atzberg@gmail.com; website: http://atzberger.org/

August 4, 2017

We investigate electrolyte-mediated interactions of charged analyte particles confined within nanochannels. We investigate how the free energy of analyte particle position varies with ionic strength and ion valence for multivalent 2:1 electrolytes and monovalent 1:1 electrolytes. Our studies use a particle-based Restrictive Primitive Model (RPM), classical Density Functional Theory (cDFT), and mean-field Poisson-Boltzmann Theory (PB). We assess for the nanochannel system the modeling fidelity of cDFT and PB relative to RPM. We find for sufficiently charged regimes that interesting features in the free energy profile can develop with energy barriers and a minimum giving a preferred localization of a charged analyte particle near the walls of the nanochannel. We discuss the underlying origins of these behaviors by statistically characterizing the contributions of overcharging, overlap of ionic double-layers, and ion-ion correlations. We also discuss how our results may be used to further improve models of confined electrolytes and more generally their implications for phenomena in nanoscale devices.

1. Introduction

In microscale and nanoscale systems the electrostatics of the associated electrolyte and charged objects can exhibit subtle collective behaviors that play a central role in equilibrium phase behavior and kinetics. This includes transitions in the stability of colloidal suspensions [9,20,56], electrophoretic separation and detection in fluidic devices [5,25,26,41,50], and biomolecular interactions [3,33,52]. Confinement of electrolytes and objects between charged walls present additional contributions often resulting in rich phenomena that are particularly important to nanoscale systems. This owes to the thickness of ionic layers often being comparable to other length-scales in the system [4,8,19,25]. When the charge interactions become sufficiently strong there are interesting theoretically predicted and experimentally observed phenomena that can arise. This includes the formation of condensed ion layers on surfaces, over-charging of walls and particles, and attractions between like-charged objects [29,30,47]. These effects have formed the basis for understanding phenomena such as DNA condensation [6,27,28,49,51], colloidal stability [20,29,37], and attraction of like-charged plates [24,35,40]. We further explore here phenomena of strongly charged systems in the context of analyte particles confined within nanochannels. We investigate the behaviors of confined electrolytes and charged particles through simulations of a Restrictive Primitive Model (RPM) and through

* Work supported by DOE ASCR CM4 DE-SC0009254, W.M. Keck Foundation, NSF CAREER Grant DMS-0956210, and NSF DMS - 1616353.

classical Density Functional Theory (cDFT). We investigate the interactions between a charged analyte particle and the nanochannel wall as the electrolyte concentration and particle charge are varied.

We find that in some charge regimes the free energy of the particle as a function of its position within the channel develops a significant minimum in a preferred location near the nanochannel wall. Interestingly, in some regimes this preferred location is separated from the nanochannel center by a significant energy barrier. Motivated by nanofludic devices our results indicate that analyte particles could exhibit interesting bi-modalities, switching between long dwell times in locations near the channel center with locations near to the channel wall. For instance, this could have implications for experimental protocols and devices such as capillary electrophoresis used in fluidics for separations and detection [25, 41, 50, 57].

We investigate the free energy of the analyte particle as the ionic strength and the valence of ions in the electrolyte are varied. We further investigate the origins of the free energy profile by using our RPM approach to characterize at the coarse-grained molecular-level the condensed ionic layers than form near the wall and particle surface and also the ion-ion correlations. We further make comparisons with predictions of cDFT. While the cDFT provides helpful predictions for the double-layer structure and free energy in qualitative agreement with the RPM results, there is a significant underestimation of the strength of effects such as the free energy well depth in the most strongly charged regimes. The combined RPM and cDFT results show for the free energy profile of a confined particle the significant roles played by ion-ion correlations and over-charging at both the charged walls and analytic particle surface. We also show in the strongly charged regimes considered that a mean-field theory such as Poisson-Boltzmann theory is not adequate in predicting system behaviors.

We introduce our RPM model for the electrolyte and analyte particle in Section 2.1. We introduce our cDFT description of the nanochannel system in Section 2.2. We present the results of our calculations including the counterion and coion densities, analyte particle free energy, and ion-ion correlation functions in Section 3. We discuss our findings and related phenomena observed within nanochannels in Section 4. Additional information on the computational methods developed and simulation protocols are discussed in the Appendix.

2. Electrostatics of the Nanochannel System

2.1. Restrictive Primitive Model (RPM)

We consider an analyte particle confined within a nanochannel having a slit-like geometry with the walls of the channel corresponding to two like-charged parallel plates. We consider electrolytes consisting of both counterions and coions, using a coarse-grained model related to the Restrictive Primitive Model (RPM) [53–55] where discrete ion-ion interactions are taken into account within a continuous dielectric medium. A snapshot of the system is shown in Fig. 1. We model the finite size of the ions and the excluded volume of the analyte particle using the Weeks-Chandler-Andersen (WCA) interaction potential [58]

$$\phi_{\text{wca}}(r) = \begin{cases} 4\epsilon\left[(b/r)^{12} - (b/r)^{6} + \frac{1}{4}\right], & r \le r_c \\ 0, & r > r_c. \end{cases} \tag{1}$$

where r is the distance between the center-of-mass of the two particles. For a particle with steric radius b we have $r_c = 2^{1/6} \cdot b$. This ensures a purely repulsive interaction between particles [58]. For the steric particle-wall interactions, we use the Lennard-Jones 9-3 potential

$$\phi_{\text{lj93}}(r) = \epsilon\left[\frac{2}{15}(b/r)^{9} - (b/r)^{3}\right]. \tag{2}$$

Here, r denotes the distance between a particle and the wall. Electrostatic interactions between ions and/or the analyte particle of charge q_1 and q_2 are given by the Coulomb interaction

$$\phi_{\text{coul}}(r) = \frac{q_1 q_2}{4\pi\epsilon_0 \epsilon r} \tag{3}$$

where ϵ is the dielectric constant of the background medium and we use SI units.

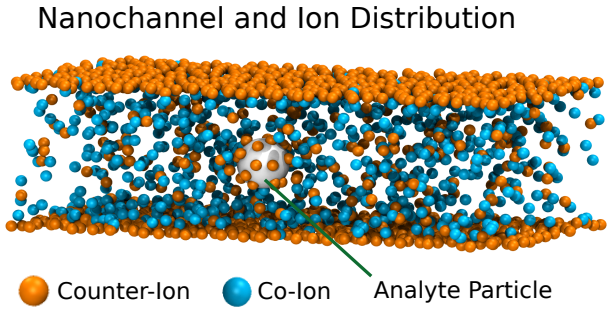

Figure 1: *Analyte Particle Confined within a Nanochannel. We consider an electically neutral electrolyte at the level of individual finite sized ions. Shown is a cut-away view of the electrolyte and analyte particle corresponding to $\sigma = -6$ and $C_m = 8$ with counterions with $+2$ charge (orange) and coions with -1 charge (blue). Strong correlations are exhibited where counterions and coions form clusters and chains throughout the electrolyte and layers near the wall and analyte particle surface.*

To handle the long range Coulumb interaction we use the Particle-Particle Particle-Mesh (PPPM) approach [23, 43] as implemented in LAMMPS [42]. For the nanochannel with slit geometry we use a variant of the PPPM method which uses periodic boundary conditions in the xy-directions [60]. To account for the surface charge σ of the analyte particle we use Gauss' Law [17] allowing us to use a point charge Q_0 at the center-of-mass with $Q_0 = 4\pi R^2 \sigma$, where R is the radius of the particle.

We remark that any surface charge of the two walls does not generate a net electric field that acts on the ions when the walls are parallel and have a uniform equal continuous charge. The charge of a wall contributes to the electric potential for ion interactions as

$$\phi_{\text{coul-w}}(z) = \int \frac{q_1 \sigma}{\epsilon |z\mathbf{e}_z - \mathbf{r}'|} dxdy, \tag{4}$$

where $\mathbf{r}' = x\mathbf{e}_z + y\mathbf{e}_z$. The $\mathbf{e}_i$ denotes the standard basis vector pointing in the i^{th} coordinate direction. For a constant uniform surface charge σ this can be integrated to obtain the equivalent potential

$$\phi_{\text{coul-w}}(z) = -(2\pi q_1 \sigma/\epsilon) z. \tag{5}$$

For two equally charged parallel walls the net electric field $E = -d\phi/dz$ acting on ions confined between the walls is zero. This follows since

$$\begin{aligned} \phi(z) &= \phi_{\text{coul-w}}(z) + \phi_{\text{coul-w}}(L - z) \\ &= -(2\pi q_1 \sigma/\epsilon)(z + L - z) \\ &= -(2\pi q_1 \sigma/\epsilon) L. \end{aligned} \tag{6}$$

The ion-wall Coulombic potential is independent of z and constant for all locations of the ion. The electric field exactly balances between two ideal uniformly charged parallel walls and the ion experiences no net force $F = -\partial_z \phi(z) = 0$. Interestingly, this cancellation does not hold in the case of two walls that have a finite extent or non-uniform surface charge. This can be seen by integrating equation 4 in polar coordinates for two disk-like walls of radius R. However, here we simulate a system with infinite length walls (through periodic boundary conditions) and so we do not place any explicit charges on the walls.

As we shall discuss in more detail, a double layer of ions forms near the walls, resulting in an effective wall surface charge density. The double-layers should be viewed as arising not from wall attractions but rather from the confinement of the ions. The presence of the wall breaks symmetry with ions residing on only one side. Since the like charges repel one another within the confined

region and there are no balancing forces from ion charges on the other side of the walls the like-charge repulsion results in ions being pushed from the interior towards the walls in a manner similar to an osmotic pressure [2,59]. It is in this manner that double-layers arise in a system with equally charged (or neutral) walls.

In some of the simulations, we use a harmonic potential to hold the analyte particle at a given location by

$$\phi_{\text{target}}(\mathbf{x}) = \frac{k}{2}\left|\mathbf{x}-\mathbf{x}_0\right|^2, \tag{7}$$

where $\mathbf{x}_0$ is the target location for the analyte particle location $\mathbf{x}$. The total potential energy associated with a configuration of the nanochannel system including the counterions, coions, and analyte particle is given by

$$\Phi[\mathbf{X}] = \Phi_{\text{coul}}[\mathbf{X}] + \Phi_{\text{sterics}}[\mathbf{X}] + \Phi_{\text{target}}[\mathbf{X}], \tag{8}$$

where we represent the configuration of analyte particle and ions by the composite vector $\mathbf{X} = [\mathbf{X}_{\text{analyte-particle}}, \mathbf{X}_{\text{ions}}]^T$. To sample equilibrium configurations we use Langevin dynamics [13]

$$m\frac{d\mathbf{V}}{dt} = -\gamma\mathbf{V} - \nabla\Phi[\mathbf{X}] + \mathbf{F}_{thm}, \tag{9}$$

where $d\mathbf{X}/dt = \mathbf{V}$ and $\left\langle \mathbf{F}_{thm}(s)\mathbf{F}_{thm}^T(t)\right\rangle = 2k_BT\gamma\delta(t-s)$. Parameter values that we use in our simulations are given in Table 1.

Parameter	Value
ℓ_z nanochannel width (z)	6 nm
ℓ_x, ℓ_y nanochannel length (x,y)	18 nm
σ_w wall surface charge	-0.72 e/nm^2
b_w wall steric parameter lj93	0.5 nm
$r_c^{[w]}$ wall cut-off parameter lj93	0.425 nm
ϵ_w wall energy lj93	2.27e+7 $amu\ nm^2/ns^2$
σ particle surface charge	-3 e/nm^2
R particle radius	0.75 nm
m_0 particle mass	6.20e+3 amu
T temperature	300 K
k_BT thermal energy	2.50e+6 $amu\ nm^2/ns^2$
ρ solvent mass density	6.02e+2 amu/nm^3
μ solvent viscosity	5.36e+5 amu/(nm·ns)
ϵ_r solvent relative permittivity	80.1
b_- counterion radius	0.116 nm
b_+ coion radius	0.116 nm
q_- counterion charge	-1 e
q_+ coion charge	+2 e
m_- counterion mass + solvantion	2.3e+1 amu
m_+ coion mass + solvantion	2.3e+1 amu
$\bar{c}_-$ reference ion concentration	0.214M
$\bar{c}_+$ reference ion concentration	0.128M
$r_c^{[w]}$ wall LJ cutoff	0.425 nm
$r_c^{[c]}$ coulombic cutoff	6 nm
Δt Langevin timestep	1.0e-5 ns
γ Langevin drag	$6\pi\mu R$
τ_e Langevin equilibration time	0.5ns

Table 1: *Parameter values for the nanochannel model. We use by default these values unless specified otherwise.*

2.1.1. Model parameters

We investigate the structure of the double-layer as the strength of charge of the analyte particle and as the ion concentrations are varied. We mostly focus on divalent cations with $q_+ = 2e$ and monovalent anions with $q_- = -1e$. We characterize the charge of the negatively charged analyte particle Q_{particle} in terms of its surface charge density σ, where $Q_{\text{particle}} = 4\pi R^2\sigma$. We take as a reference concentration for the counterions $\bar{c}_+ = 0.128M$ and for the coions $\bar{c}_- = 0.214M$, expressed in molar units. Other ion concentrations are a multiple C_m of these baseline reference concentrations. For example, $C_m = 10$ corresponds to a counterion concentration $c_+ = C_m\bar{c}_+ = 1.28M$ and a coion concentration $c_- = C_m\bar{c}_- = 2.14M$. The simulations are performed with a fixed number of ions, with an excess of counterions so that the bulk electrolyte solution (in the absence of the analyte particle) is not neutral. The excess counterions (cations) lead to an effective negative charge on the nanochannel walls, given by the

condition of overall electric neutrality:

$$q_- N_- + q_+ N_+ + Q_{\text{particle}} + 2Q_{\text{wall}} = 0. \tag{10}$$

The $N_- = Vc_-$ and $N_+ = Vc_+$ denote the number of ions in the unit cell where V is the channel volume. The Q_{wall} is the charge on each wall in the unit cell. For a given fixed concentration of coions and counterions the effective surface-charge of the wall is obtained from electric neutrality by solving for Q_{wall} in equation 10.

We performed simulations for analyte particles with surface charges of σ = -1, -3, and -6 e/nm^2; for brevity we will refer to these three cases without units, as the systems with σ = -1, -3, and -6. As described in Section 2.1, the nanochannel walls develop a surface charge due to the ion interactions in the nanochannel. The wall surface charge density for each system simulated is given in units of e/nm^2 in Table 2. The wall charge density increases with increasing ion concentration. Additionally, the wall surface charge densities vary slightly depending on the analyte particle charge, since we have a fixed number of ions in the channel.

	$\sigma = -1$	$\sigma = -3$	$\sigma = -6$
$\mathbf{C_m = 1}$	-0.74	-0.72	-0.68
$\mathbf{C_m = 2}$	-1.49	-1.46	-1.43
$\mathbf{C_m = 4}$	-2.98	-2.96	-2.93
$\mathbf{C_m = 6}$	-4.48	-4.46	-4.43
$\mathbf{C_m = 8}$	-5.98	-5.95	-5.92
$\mathbf{C_m = 10}$	-7.47	-7.45	-7.42

Table 2: *Wall Surface Charge Density (units are e/nm^2). For the different regimes considered, we give the implicit surface charge density that arises from electric neutrality given by the condition in equation 10.*

In the regimes we consider, the electrostatic interactions vary in strength. We can characterize the strength of the interactions by the electrostatic coupling constant [34] given by

$$g \equiv 2\pi q^3 \ell_B^2 \sigma. \tag{11}$$

The $q = 2e$ is the charge of the divalent counterions and σ is the charge density of either the analyte particle or the channel walls. The Bjerrum length ℓ_B, the distance at which the electrostatic interaction energy is comparable to the thermal energy $k_B T$, is $\ell_B \equiv e^2/4\pi kT\epsilon\epsilon_0$. In our systems with divalent cations, the electrostatic coupling constant ranges from $g \approx 17$ for the least charged system, up to $g \approx 188$ for the most strongly charged system. Previous studies of electrolytes near flat surfaces [34] have shown that the counterion density profiles agree with the PB theory for $g \approx 1$, the profiles show clear deviation from PB theory for $g = 10$ and $g = 100$, and they show good agreement with the strong-coupling limit for $g = 10^4$ see [34]. Previous simulations of highly charged spheres explored coupling constants ranging from $g = 26$ up to $g = 615$ and found attraction between like-charged spheres [1, 18, 48]. We therefore expect our simulations to be in the intermediate regime between weak and strong coupling.

2.2. Classical Density Functional Theory (cDFT)

In the classical density functional theory (cDFT) calculations, we model the ions as interacting charged hard spheres with diameters d_α and charges q_α. We represent the analyte particle as a larger hard sphere of radius R that has surface charge density σ. The ions are treated as mobile fluid species, while the analyte particle has a fixed spatial location. We treat the solvent as a uniform background dielectric medium. We account for the steric interactions between the ions and the analyte particle using a hard sphere interaction $V(r) = \infty$ for $r < R$, where r is the distance between the ion and the center of the analyte particle. In addition, we add a smooth truncated potential based on the Lennard-Jones

(LJ) interaction to the surface of the analyte particle,

$$V_\alpha^{mLJ}(r') = 4\epsilon_m \left[\left(\frac{\sigma_m}{r'}\right)^{12} - \left(\frac{\sigma_m}{r'}\right)^{6} \right], \quad (12)$$

where r' is the distance between the ion and the surface of the analyte particle. We truncate and shift this potential to obtain

$$V_\alpha^{m}(r') = V_\alpha^{mLJ}(r') - V_\alpha^{mLJ}(r_c'), \quad r' < r_c', \quad (13)$$

with $V_\alpha^m(r') = 0$ for $r' > r_c'$, at large distances from the analyte particle. In our notation, the subscript α refers to the index of the particular ion species and the mLJ and m to the modified Lennard-Jones potentials. This repulsive potential serves to smooth the surface of the analyte particle to reduce mesh-size effects in our discretized cDFT. We used $\epsilon_m = 0.5 k_B T$ and $\sigma_m = d$ (where d is the ion diameter) for all calculations. The channel boundaries are modeled as hard walls with the interaction potential for the ions

$$V_\alpha^w(z) = \begin{cases} \infty, & \text{ions outside the channel} \\ 0, & \text{ions inside the channel.} \end{cases} \quad (14)$$

We use a formulation of cDFT that follows closely the work of Oleksy and Hansen [38] and is very similar to that of Henderson et al. [21]. We formulate the cDFT for an open ensemble, specified by the temperature T, the total volume V, and the chemical potentials μ_α of all fluid species in the system. We discuss the relation of these parameters to the RPM model in Section 2.2.1.

The grand free energy of the system is given as a functional of the ion densities $\rho_\alpha(\mathbf{r})$:

$$\Omega[\rho_\alpha(\mathbf{r})] = \sum_\alpha F[\rho_\alpha(\mathbf{r})] \quad (15)$$

$$- \sum_\alpha \int d\mathbf{r} \left(\mu_\alpha - V_\alpha(\mathbf{r})\right) \rho_\alpha(\mathbf{r}). \quad (16)$$

For notational convenience, it is to be understood that $\Omega[\rho_\alpha(\mathbf{r})]$ depends on all of the density fields $\{\rho_\alpha\}$ collectively, where we use this convention to reduce clutter. Here $F[\rho_\alpha(\mathbf{r})]$ is the intrinsic Helmholtz free energy of the system. $V_\alpha(\mathbf{r}) = V + V^m + V^w$ denotes the neutral part of the potential that acts on each ion from the walls and the analyte particle. The equilibrium density profile $\rho_\alpha^0(\mathbf{r})$ minimizes the free energy functional $\Omega[\rho_\alpha(\mathbf{r})]$. This can be expressed in terms of the variational derivative [14]

$$\left.\frac{\delta\Omega[\rho_\alpha(\mathbf{r})]}{\delta\rho_\alpha(\mathbf{r})}\right|_{\rho_\alpha^0} = 0. \quad (17)$$

At equilibrium the associated grand potential free energy of the system is $\Omega^0 = \Omega[\rho_\alpha^0(\mathbf{r})]$ [10]. The intrinsic Helmholtz free energy we use consists of four terms given by

$$\begin{aligned} F[\rho_\alpha(\mathbf{r})] &= F_{id}[\rho_\alpha(\mathbf{r})] + F_{hs}[\rho_\alpha(\mathbf{r})] \quad (18) \\ &+ F_{coul}[\rho_\alpha(\mathbf{r})] + F_{corr}[\rho_\alpha(\mathbf{r})]. \end{aligned}$$

The terms represent respectively the Helmholtz free energies for the ideal gas (id), hard spheres (hs), mean-field Coulombic interactions (coul), and second order charge correlations (corr). In formulating the DFT, approximations are needed to capture each of the listed effects. We briefly discuss each of the terms and give more details in Appendix A.

The term F_{id} corresponds to the contributions of an ideal gas which for a given density is known exactly and is given in Appendix A. For the hard-sphere interactions F_{hs}, we use the *White Bear* version of the fundamental measure theory [45]. The mean-field Coulombic interaction F_{coul} is given by integrating the collective electric potential and density of the ionic species, see Appendix A. The charge correlation term F_{corr} is based on a functional Taylor expansion of the direct correlation function, which in turn is obtained from the known analytic solution of the mean-spherical approximation (MSA) for mixtures of charged hard spheres given in [38]. Detailed expressions for each of these free energy terms are given in Appendix A.

Minimization of the grand free energy in equation 15 with respect to the density profiles of each ionic species is expressed mathematically as a set of nonlinear partial differential-integral Euler-Lagrange (EL) equations. We express this in terms of residual equations $R_i = 0$ where

$$\begin{aligned} R_1 &= \ln \rho_\alpha(\mathbf{r}) + V_\alpha(\mathbf{r}) - \mu_\alpha \\ &+ \int \sum_\gamma \frac{\partial \Phi}{\partial n_\gamma}(\mathbf{r}')\omega_\alpha^{(\gamma)}(\mathbf{r}-\mathbf{r}')d\mathbf{r}' \\ &- \sum_\beta \int d\mathbf{r}' \rho_\beta(\mathbf{r}')\Delta c_{\alpha\beta}(\mathbf{r}-\mathbf{r}') + Z_\alpha \phi(\mathbf{r}) \end{aligned} \tag{19}$$

$$R_2 = n_\gamma(\mathbf{r}) - \sum_\alpha \int d\mathbf{r}'\, \rho_\alpha(\mathbf{r})\omega_\alpha^{(\gamma)}(\mathbf{r}-\mathbf{r}') \tag{20}$$

$$R_3 = \nabla^2\phi(\mathbf{r}) + \frac{4\pi\ell_B}{d}\sum_\alpha q_\alpha \rho_\alpha(\mathbf{r}) \tag{21}$$

Here ϕ is the electric potential; other terms are defined in Appendix A. The residual equations are solved computationally within the spatial domain of the nanochannel. The third residual equation R_3 is Poisson's equation for the electrostatic potential $\phi(\mathbf{r})$. The cDFT calculations are performed using the open source package Tramonto, available at https://github.com/Tramonto/Tramonto. The EL equations are solved in real-space on a Cartesian mesh using inexact Newton iterations for the density fields and a finite element method for the electrostatic potential. Details of these numerical methods and discussions of related applications of Tramonto to charged systems can be found in [11,12,22,36].

All quantities in the residual equations have been expressed in terms of reduced units with energies in units of k_BT and lengths in units of the ion diameter d. Z_α is the valence of species α. The dimensionless quantity appearing in R_3 is sometimes called the plasma parameter or the reduced temperature, $T^* = d/\ell_B$.

2.2.1. Parameterization

We parameterized our cDFT calculations to yield results in comparable physical regimes as the RPM models. This was done by taking the temperature and dielectric constant so that $\ell_B = 7.1$ Å as in the RPM simulations, using the same surface charge density on the analyte particle as in the RPM, matching the ion diameters (twice the ionic radius used in the RPM), $d = 2b = 0.232$ nm, and using the radius $R = 0.75$ nm for the analyte particle. We used a channel with total width $\ell_z = 6$ nm as in the RPM model. The channel walls extend into the channel to the same distance as in the simulations, so that we match the hard wall condition in the DFT with the Lennard-Jones 9-3 repulsive walls in the simulations.

To reduce computational costs in the cDFT calculations, we placed the analyte particle with its center on the z-axis, so that the symmetry of the system allows for reflecting boundary conditions to be used in the x- and y-directions and thus only 1/4 of the particle needs to be directly included in the calculations. For this purpose, the size of the computational domain in the x and y directions was $\ell_x = \ell_y = 4.6$ nm, for an effective channel length of 9.28 nm (taking into account the reflecting boundary through the center of the particle). We used a mesh size of 0.058 nm in all the 3D calculations (i.e. a mesh size of $0.25d$ in reduced units, where $d = 0.232$ nm is the diameter of the ions).

The RPM simulations were performed in the canonical ensemble at constant N_α, V, and T. For cDFT it is more natural to work in the grand canonical ensemble at constant μ_α, V, and T. To make a correspondence between these two sets of calculations, we set the chemical potentials in the cDFT so that the average ion densities match the RPM simulations at the middle of the channel where nearly bulk conditions prevail. In the middle of the channel, the electrolyte solution is neutral, with $c_- = 2c_+$. We set the surface charge

density of the channel walls in the cDFT equal to the effective surface charge densities given in Table 2.

We solve equations (36)-(37) in the nanochannel geometry with Neumann boundary conditions on $\phi(\mathbf{r})$ at the nanochannel walls and the analyte particle, i.e. we set the charge density of these surfaces. We employ Dirichlet boundary conditions elsewhere, with a reflecting boundary through the analyte particle as described above.

To obtain the free energy associated with the particle at a particular position within the channel, we performed a cDFT calculation at each particle position and use the grand free energy of the resulting density. We computed density profiles of ions around the particle both in the case with the particle in the center of the channel and in the case with the particle in the bulk fluid with no channel present. The density profiles were found to be the same in both cases. We also found that the density profile near the channel wall, at a location in the channel far from the particle, was also independent of the presence or absence of the analyte particle. This allowed us a significant reduction in computational costs by performing calculations of the wall density profiles from 1D systems using cDFT. In our 1D calculations we used a finer mesh size of 0.0232 nm for better resolution in the reported results.

2.3. Poisson-Boltzmann (PB): Mean-Field Theory

In the limit that the ions are treated as point particles and do not have any charge correlation contribution to their free energy, the cDFT reduces to the Poisson-Boltzmann (PB) equation. The PB limit corresponds to the Helmholtz free energy functional with only the ideal gas and mean-field Coulombic contributions given by

$$\begin{aligned} \beta F[\rho_\alpha(\mathbf{r})] &= \beta F_{id}[\rho_\alpha(\mathbf{r})] + \beta F_{coul}[\rho_\alpha(\mathbf{r})] \\ &= \sum_\alpha \int d\mathbf{r} \rho_\alpha(\mathbf{r}) \left(\ln \rho_\alpha(\mathbf{r}) - 1\right) \\ &+ \sum_\alpha \int d\mathbf{r} q_\alpha \rho_\alpha(\mathbf{r}) \phi(\mathbf{r}), \end{aligned} \tag{22}$$

where $\beta = 1/kT$. Minimization of the grand free energy in equation 15 using the free energy F in equation 22 gives

$$\frac{\delta \Omega}{\delta \rho_\alpha} = 0 = \ln \rho_\alpha(\mathbf{r}) + q_\alpha \phi(\mathbf{r}) - \beta \tilde{\mu}_\alpha. \tag{23}$$

Here $\tilde{\mu}_\alpha = \mu_\alpha - V_\alpha(\mathbf{r})$ is the spatially dependent chemical potential including the contributions of the ion interactions with the channel wall and analyte particle in equation 15. Solving for the density gives

$$\rho_\alpha(\mathbf{r}) = \exp[\beta \tilde{\mu}_\alpha - q_\alpha \phi(\mathbf{r})]. \tag{24}$$

In the case that the electric potential vanishes to zero in the bulk we have $\rho_\alpha^b = \exp[\beta \tilde{\mu}_\alpha]$. However, in the nanochannel system the term ρ_α^b should be interpreted with some care. Since the steric interaction potential depends on ion location we technically have $\rho_\alpha^b(\mathbf{r}) = \exp[\beta \tilde{\mu}_\alpha(\mathbf{r})]$, which is a known function of position. However, in the limit of hard wall interactions that we use here, the PB theory can be further simplified by using boundary conditions to represent the walls and analyte particle. This eliminates the explicit dependence of $\rho_\alpha^b(\mathbf{r})$ on position. The remaining part of the chemical potential μ_α is constant and we simply have $\rho_\alpha^b = \exp[\beta \mu_\alpha]$, where ρ_α^b are the reference densities (ion densities in a reservoir in equilibrium with the nanochannel system; these are nearly identical to the ion densities in the middle of the channel).

The electric potential satisfies Poisson's equation $\nabla^2 \phi = -(4\pi \ell_B/d) \sum_\alpha \rho_\alpha$. Combining this

with the densities found in equation 24 gives the non-linear Poisson-Boltzmann equations

$$\nabla^2\phi(\mathbf{r}) = -\frac{4\pi\ell_B}{d}\sum_\alpha \rho_\alpha^b \exp[-q_\alpha\phi(\mathbf{r})]. \quad (25)$$

Here d is a reference length in the system which for convenience we take to correspond to the ion size but other choices are also possible.

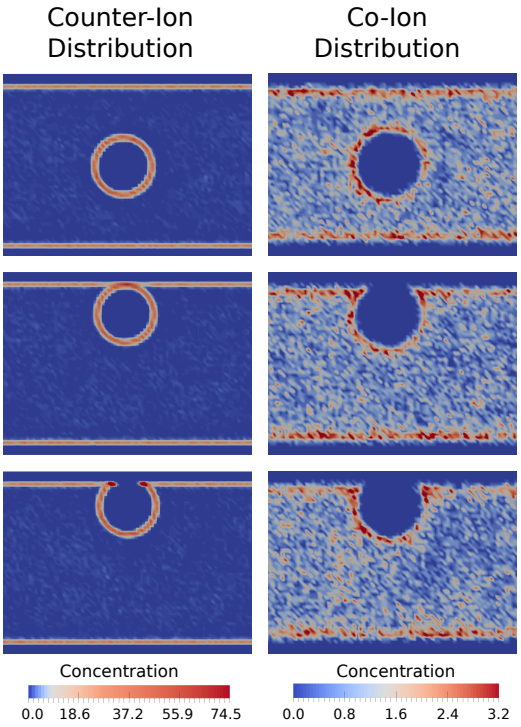

Figure 2: *Concentration of counterions and coions in the nanochannel. We show the average concentration of ions as the analyte particle position is varied within the nanochannel, at* $X_0^{(3)} = 3.0nm, 4.6nm, 4.85nm$ *for* $\sigma = -3$ *and* $C_m = 8$.

3. Results

3.1. Ionic Double-Layer Structure: Restrictive Primitive Model (RPM)

We show in Figure 2 typical distributions for the counterions and coions as the analyte particle position is varied in the case of $\sigma = -6$ and $C_m = 8$. In this regime strong layering occurs for the counterions near the walls and near the analyte particle surface. Also, a secondary layer of coions occurs offset from the walls and the analyte particle surface adjacent to the counterion layer. This is especially visible for the coions shown in the right panel of Figure 2.

We show the ion concentrations near the wall for $\sigma = -6$ and varying C_m in Figure 3. The other cases with $\sigma = -1$ and $\sigma = -3$ show ion concentrations that are indistinguishable after scaling the concentration with the case with $\sigma = -6$. For ions near the wall there are two length scales associated with the ion layers. The first length scale is the location of the closest ion layer to the wall, which occurs at the minimum of the Lennard-Jones potential of equation 2, at $\ell_* = (18/45)^{1/6} b_w = 0.43$ nm. From the steric interactions the next closest layer can form only around $\ell_2 = \ell_* + b_+ + b_-$. For the parameters in Table 1 we have $\ell_2 = 0.66$ nm. We see both of these length-scales manifest in the structure of the ion layers. The double-layer essentially forms according to the packing distance imposed by the

ion and wall sterics. This becomes especially pronounced as the concentration increases as seen in Figure 3.

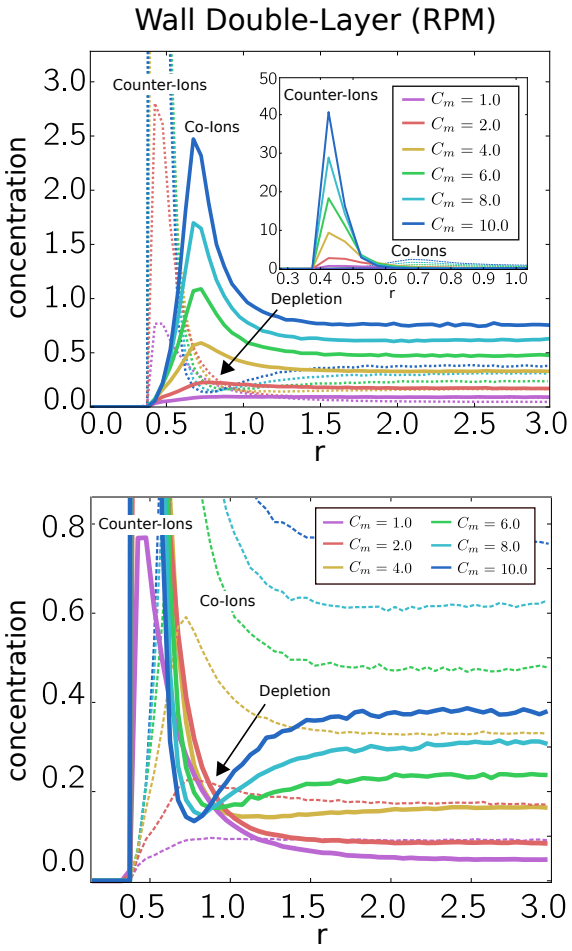

Figure 3: *Wall Double-Layer. Ion concentrations near the channel walls (RPM) as C_m is varied, for $\sigma = -6$.*

Other interesting features arise in the ion layers near the wall as the ion concentrations increase. The ion layers become smaller in width and more dense as the ion concentration increases. For small concentrations there is significant overlap between the counterion and coion layers with significant mixing of ions especially within the secondary coion layer. As the concentration increases the layers become more distinct. Interestingly, for the counterion layer depletion occurs for the counterions within the secondary layer relative to the counterion concentration in the bulk. This is especially pronounced once $C_m > 4$ as shown in the inset in Figure 3. For $C_m < 4$ the concentration of the counterions appear to monotonically decay to the bulk counterion concentration.

In the nanochannel in the regimes we consider the ion double-layer structure is in contrast to many theories developed for weakly charged systems with a proposed stern layer and Helmholtz plane demarcating a transition from relatively immobile ions to a gaseous mobile phase of ions [5,25]. From that perspective for our system at high ion concentrations this transition effectively occurs on the length scale of individual ions. Near the wall the surface counterion and coion positions are strongly correlated, as shown in the simulation snapshot in Figure 4. Many of the ions form pairs with opposing ions or small clusters or chains. The wall surface is covered in a condensed layer of counterions along with a secondary layer of coions that forms as part of clusters near individual counterions, see Figure 4. This indicates some of the challenges involved in developing theory for such highly charged and concentrated regimes, where behaviors may be dependent on individual ion-ion interactions and charge clusters containing only a few ions.

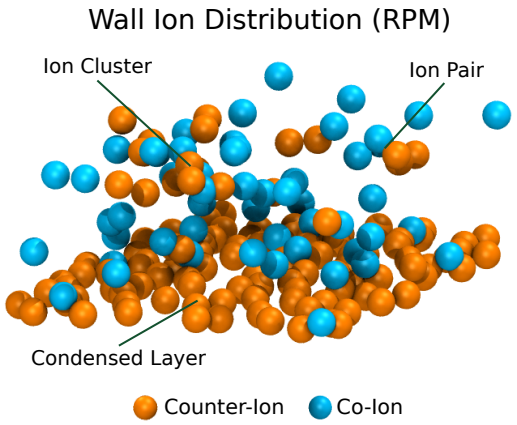

Figure 4: *Ion configurations near the wall (RPM), for* $\sigma = -6$ *and* $C_m = 8$.

Next we show the density of counterions and coions near the analyte particle surface for the three different surface charges $\sigma = -1$, $\sigma = -3$, and $\sigma = -6$ in Figure 5, Figure 6, and Figure 7. The concentrations are measured at distances relative to the analyte particle surface. The relevant steric length-scale for the position of the counterion layer in this case is the steric length $\ell_{**} = 2^{1/6}(R + b) - R = 0.22$ nm. The coion layer forms at a distance corresponding to $\ell_{2*} = \ell_{**} + 2b_{\pm} = 0.45$ nm. Again the layer locations are primarily determined by the packing of the ions as determined by the sterics.

For a relatively weak particle charge density of $\sigma = -1$, the counterions form a tight layer near the analyte particle surface with significant mixing of coions into this primary layer. After this layer the coions exhibit concentrations that rapidly approach a level comparable to the bulk, see Figure 5. For $\sigma = -3$ the counterions also form a tight layer near the analyte particle surface but with relatively little mixing of coions into this primary layer, see Figure 6. The coions show only a weak secondary peak. For the highest surface charge density of $\sigma = -6$, a secondary layer of coions forms. For the largest concentrations some depletion of the counterions is exhibited in the secondary layer relative to the bulk. This is less pronounced than in the case of the walls due to the high curvature of the particle, but can be seen readily in the case with $\sigma = -6e/nm^2$ and $C_m = 10$ as highlighted in the inset in Figure 7.

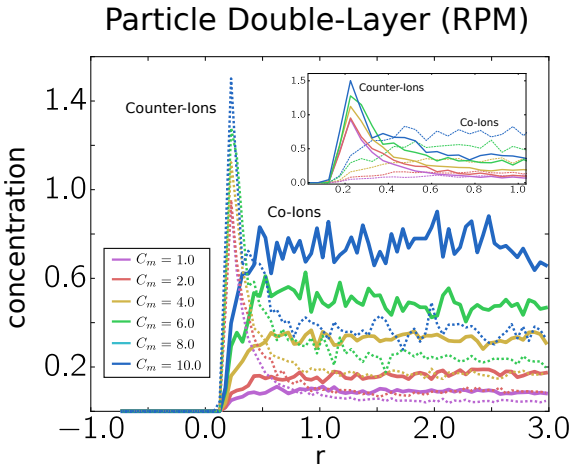

Figure 5: *Analyte Particle Double-Layer (RPM)* ($\sigma = -1.0$).

For the smaller concentrations there is significant overlap of the counterion layer with the coion layer, with significant mixing in the secondary layer. From examining configurations of the ions around the analyte particle we find this arises from strong correlations between the counterions and coions resulting in the formation of transient charge clusters, as shown in Figure 8. As the analyte particle charge increases, the layer of counterions near the particle adheres more strongly and the clusters are pushed increasingly toward the secondary layer. For the case $\sigma = -6$ this is especially pronounced with the double-layer providing excess charge relative to what would be required to achieve local electric neutrality. This over-charging phenomenon can be seen in Figure 9.

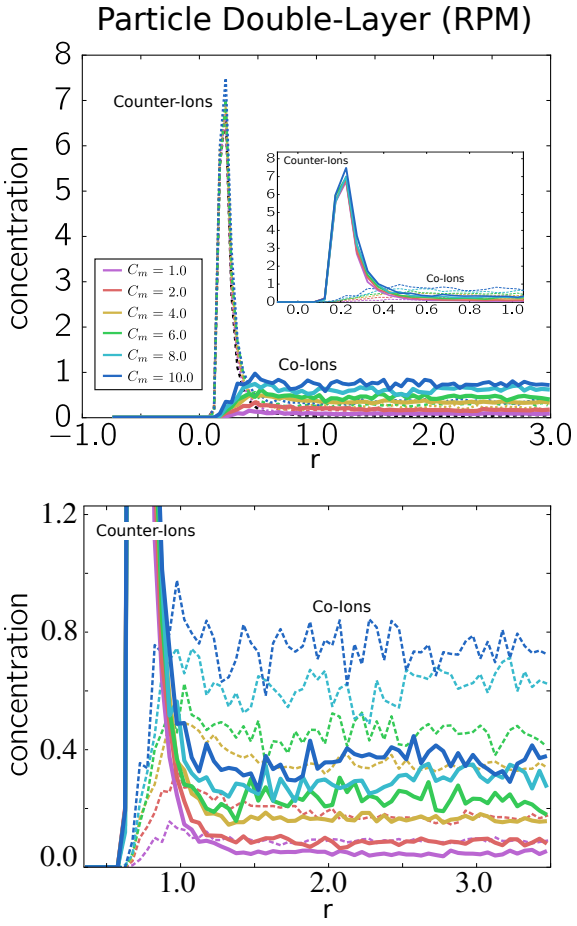

Figure 6: *Analyte Particle Double-Layer (RPM)* ($\sigma = -3.0$).

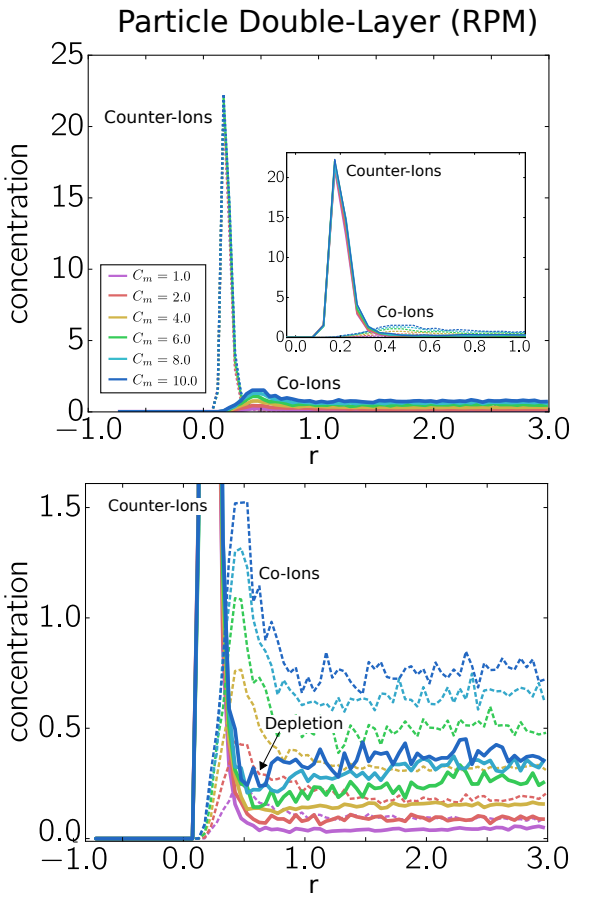

Figure 7: *Analyte Particle Double-Layer (RPM)* ($\sigma = -6.0$).

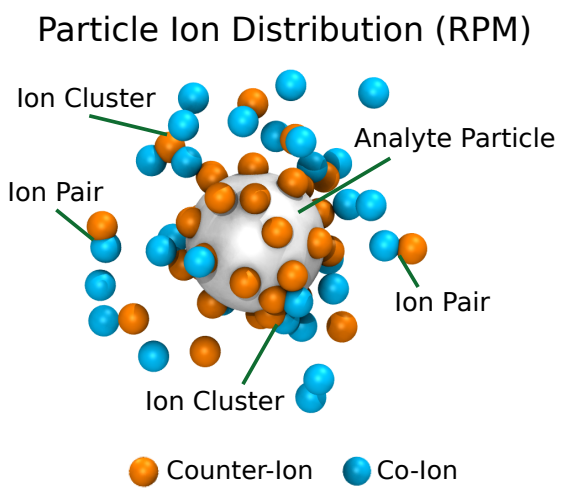

Figure 8: *Ion configurations near the analyte particle (RPM) in bulk, for $\sigma = -6$ and $C_m = 8$, showing ion pairs and clusters.*

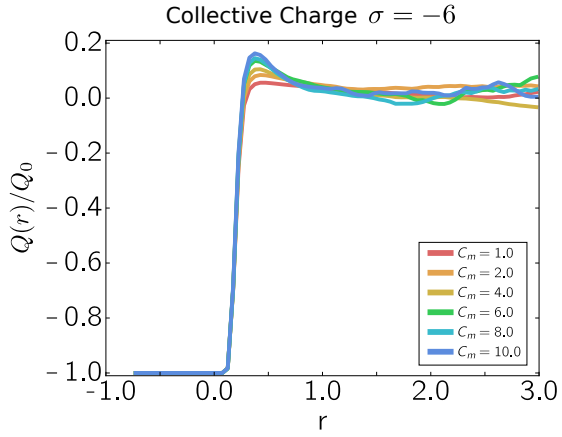

Figure 9: *Collective Charge of Analyte Particle with Double-Layer ($\sigma = -6$). The total collective amount of charge $Q(r)$ contained within the spherical volume of radius r around the analyte particle. Near the particle surface the double-layer provides excess charges (over-charging) when countering the analyte particle charge. The Q_0 is the analyte particle charge.*

3.2. Free Energy of Analyte Particle Location: Restrictive Primitive Model (RPM)

We next consider the free energy $E(d)$ of the system as a function of the analyte particle position d, see Figure 10. The wall and the analyte particle are both negatively charged, and the free energy is repulsive when the particle is sufficiently close to the wall. As the concentration of the counterions and coions becomes sufficiently large, attraction occurs between the like-charged analyte particle and wall. The free energy minimum occurs at a distance comparable to the interaction length-scale of the first layers of ions of the wall and the analyte particle surface. The sum of the length-scale for the first counterion layer of the wall $\ell_* = 0.43nm$ and the length-scale of the counterion layer of the analyte particle $\ell_{**} = 0.22nm$ is $\ell = \ell_* + \ell_{**} = 0.65nm$, corresponding to $\bar{d}/\frac{1}{2}L \sim 0.22$, the approximate location of the free energy minima in Figure 10. The free energy minimum can become significant compared to k_BT at sufficiently large C_m. We discuss this further in Section 4.

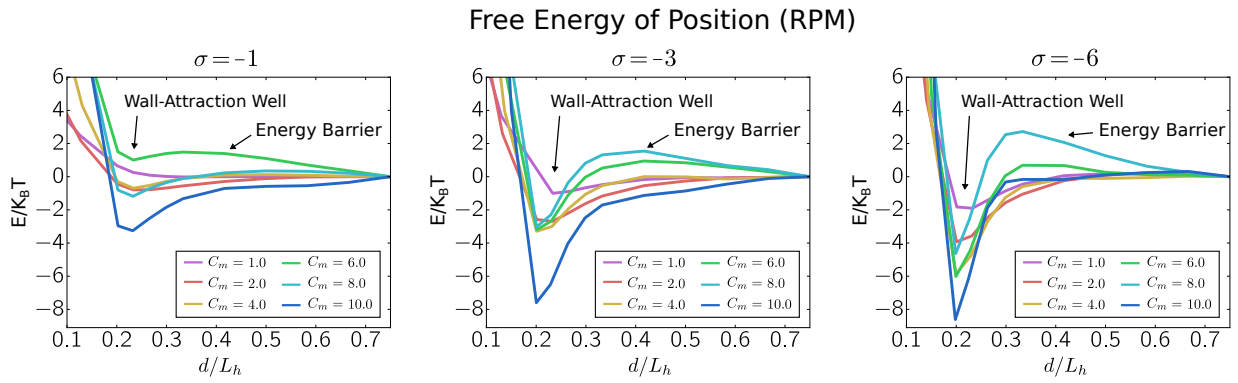

Figure 10: *Analyte Particle Free Energy (RPM) for σ = -1.0. -3.0, and -6.0, as a function of the distance d between the particle and the wall, normalized by the half-width $L_h = \frac{1}{2}L$ of the nanochannel.*

The free energy profile has an interesting non-monotonic dependence on the analyte particle charge and electrolyte ion concentrations. We see the depth of the free energy minimum well that forms near the wall is not entirely monotonic as the ionic concentration increases. Most clearly, for $\sigma = -6$ the magnitude of the free energy well depth is larger for $C_m = 6$ than for $C_m = 8$, but then increases significantly for $C_m = 10$. There is also a significant free energy barrier as large as $2k_BT$ that can arise separating the particle from the free energy local minimum near the wall. Making this even more interesting is that the largest energy barriers appear to occur for the intermediate ionic concentrations considered. For instance see the cases with $\sigma = -3, -6$ and $C_m = 8$. The free energy barrier appears to arise from the condensed ion layers that form on the analyte particle surface and wall surface that must coordinate and rearrange as the particle approaches the wall, see Figure 11.

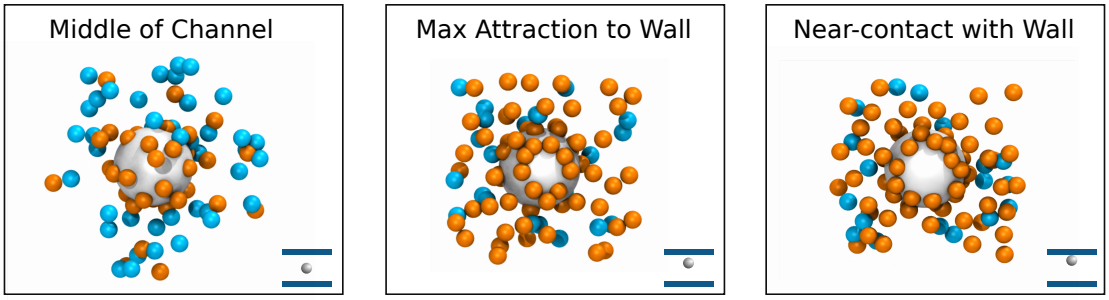

Figure 11: *Top-Down View of Analyte Particle and Ion Distribution. We show some typical distributions of ions nearby the analyte particle at different locations within the nanochannel. We show the locations corrresponding to the (i) middle of the channel at $X_0^{(3)} = 3.0nm$, (ii) maximum attraction to the wall at $X_0^{(3)} = 4.6nm$, and (iii) near-contact with the wall having large repulsion at $X_0^{(3)} = 4.85nm$.*

When the particle is at the free energy minimum, the counterions in the condensed layer typically form transient ring-like structures near the surface of the analyte particle as shown in Figure 11. These counterions appear to serve double-duty in the condensed layer by screening both the analyte particle charge and the effective wall charge. This double-duty appears to be the source of the resulting free energy gain. When the analyte particle is positioned at an even closer distance to the wall it penetrates into the condensed counterion layer. This excludes counterions which results in a significant pressure on the analyte particle surface resulting in a strong free energy penalty. It is important to remark that the effective electric field from the walls cancel so that all interactions beyond the steric distance are mediated by the ions.

3.3. Ion-Ion Correlations: Restrictive Primitive Model (RPM)

To further understand the system, we examine the ion correlations in the condensed wall layer vs in the center of the channel. The counterions and coions exhibit strong self-correlations and cross-correlations. The structures of these correlations depend significantly on whether an ion is near the channel wall or near the channel center. As a matter of convention we refer to the ions near the channel center as being in the bulk. We characterize the correlations by calculating a radial distribution function (RDF) $g(r)$ for ions within a permissible sampling region which we refer to as in the bulk or as near the wall (see Appendix C for details). The RDFs $g(r)$ are normalized by the reference number concentration given by taking the count of all counterions or coions and dividing by the channel volume. Throughout our simulations reference values are determined from the channel volume $V = 1944$ nm^3 and from the reference number concentrations $\hat{g}_- = 250/1944 \times C_m$ nm^{-3} and $\hat{g}_+ = 150/1944 \times C_m$ nm^{-3}. We remark that since the density of ions can be large near the walls the $g(r)$ can exhibit long-range normalized bulk values that are significantly less than 1.0 and normalized wall values that are in excess of 1.0.

The RDFs in the bulk are shown in Figure 12. In the bulk, the counterion-counterion $g(r)$ shows a correlation hole, with the counterions not likely to be close together. The counterion-coion interactions show strong correlations that indicate a counterion has a cluster of coions in its proximity at a distance roughtly twice the steric distance. The coion-coion $g(r)$'s exhibit a small feature around $r = 0.5$ which appears to be related to ionic clusters that form with multiple coions associated to a common counterion. Since we have divalent counterions, it makes sense that there should roughly be two coions associated with each counterion. These results indicate that on average the bulk electrolyte consists of triples of ions with one counterion and two coions, but not larger ion clusters.

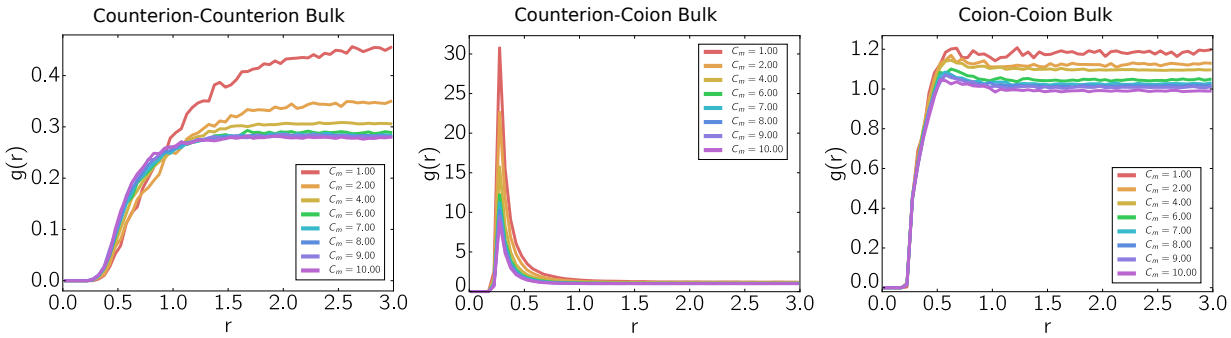

Figure 12: *Radial distribution functions $g(r)$ for ion-ion correlations in the bulk from the RPM simulations.*

Near to the wall, the RDF $g(r)$ exhibits features indicating much stronger correlations than in the bulk. While the counterion-coion correlations are similar to those in the bulk, the counterion-counterion $g(r)$ has a significant peak at small r. This is from the large density associated with the condensed counterion layer near the wall. As the charge increases there is a transition around $C_m \geq 4$ from a correlated gas-like state to a state with significant correlations that are more liquid-like [7]. The peak that develops moves closer toward the steric length-scale of the ions with peaks around 0.5 nm. The coion-coion correlations near the wall exhibit a peak for all of the regimes considered. From examining simulation trajectories we find this arises from the strong correlations of the coions with the counterions and from bulk coions that transiently move to penetrate the strongly positively-charged condensed layer. The coion-coion peak occurs independent of concentration around a similar length-scale 0.5nm as the final counterion-counterion peaks for large concentration. These results show that there are some significant differences in ion-ion correlations when near the wall relative to the bulk.

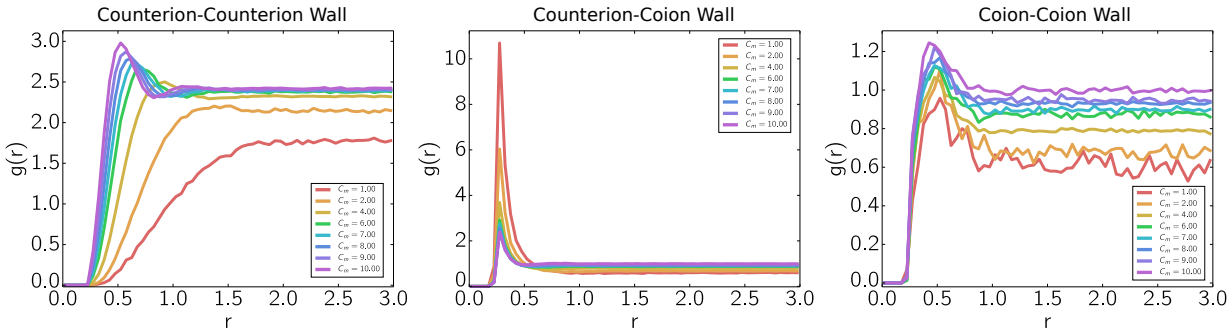

Figure 13: *Radial distribution functions $g(r)$ for ion-ion correlations near the wall from the RPM simulations.*

3.4. Results from Classical Density Functional Theory (cDFT) and Poisson-Boltzmann (PB) Theory

The classical density functional theory (cDFT) and Poisson-Boltzmann (PB) theory provide other approaches for investigating phenomena in electrolytes and charged systems that are expected to be more computationally efficient than Langevin MD simulations. However, in cDFT and PB further approximations are incurred in

modeling the underlying physics of the charged system. We expect that cDFT could provide a decent basis for describing the nanochannel system given the inclusion of terms accounting for charge correlations and ion sterics. The steric and correlation effects can be seen in the ionic layering and clustered interactions in the RPM results particularly in Figures 1 and 8. To further emphasize the importance of these effects, we include in our comparisons the mean-field Poisson-Boltzmann (PB) theory, which we do not expect to perform very well in the strongly charged regime. These results further demonstrate the importance of ion correlation effects and sterics to obtain correct phenomenology even at a qualitative level. As we shall discuss, our results further highlight the need for using descriptions beyond the mean-field theory to obtain reliable results in strongly charged regimes for the nanochannel system.

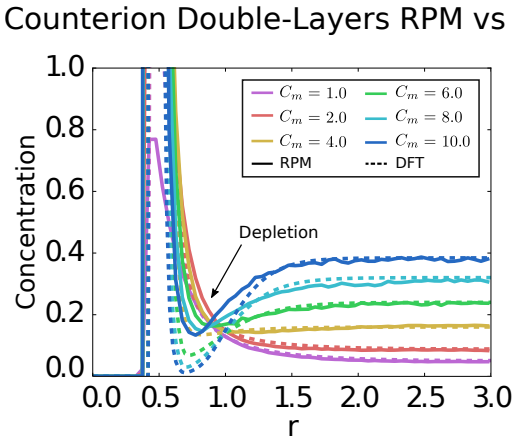

Figure 14: *Comparison of the counterion densities for the cDFT (dashed curves) and the RPM simulations (solid curves) as a function of distance r from the channel wall, for wall charge densities from the $\sigma = -6$ column of Table 2.*

We compare the ion densities near the channel walls as calculated from cDFT with the RPM density profiles in Figures 14 and 15. We find that cDFT predicts qualitatively similar trends as the RPM simulations but with some significant quantitative differences. At smaller values of C_m the profiles exhibit monotonic behavior. As observed in the RPM results, at larger values of C_m the cDFT counterion densities exhibit a distinct peak (condensed layer) followed by a depleted region before attaining the bulk counterion concentration, see Figure 14. The cDFT coion distributions exhibit a similar trend as in the RPM results with a distinct peak occurring at the location of the depleted counterion region before attaining the bulk concentration, see Figure 15. The depletion after the first layer of counterions is not seen for ion densities calculated using the Poisson-Boltzmann equation, nor for cDFT calculations with only mean-field electrostatics (i.e., without the correlation term F_{corr}). Instead, in the absence of ion correlations, the counterions exhibit a single peak near the wall that decays monotonically to the bulk, whereas the coion density profiles simply increase monotonically from the wall to their bulk concentration, with no peak.

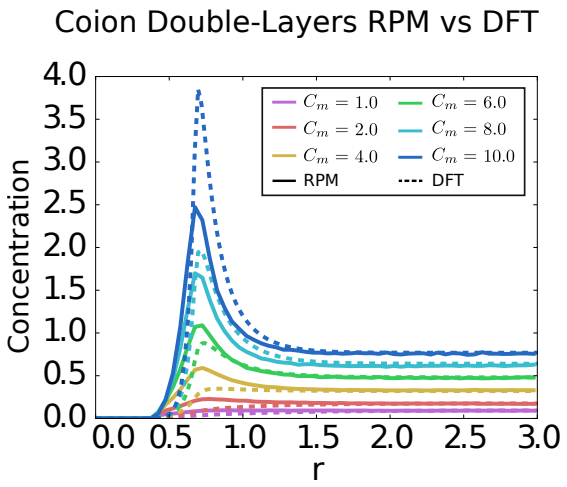

Figure 15: *Comparison of the coion densities for the cDFT (dashed curves) and the RPM simulations (solid curves) as a function of distance r from the channel wall, for wall charge densities from the $\sigma = -6$ column of Table 2.*

Thus, the cDFT charge correlation terms capture the charge density qualitatively as the ionic

concentration is varied, but as the system becomes more strongly charged there are some significant quantitative deviations with the RPM results. Compared to the RPM results, at smaller C_m the cDFT underestimates the magnitude of the coion peak but is in fairly good agreement with the long-range behavior of the counterion density profiles. At larger values, $C_m > 6$, the cDFT overestimates the magnitude of the coion peak and also overestimates the amount of depletion in the counterion density. For all concentrations and wall charge densities, the cDFT overestimates the countertion contact density at the charged wall as compared with the RPM (not shown).

Similar behavior is seen for the ion concentrations around the analyte particle, as shown in Figures 16 and 17 for $\sigma = -3$. The cDFT underestimates the magnitude of the coion peak, especially for $C_{mult} = 4$, and again overestimates the magnitude of the counterion contact density (not shown).

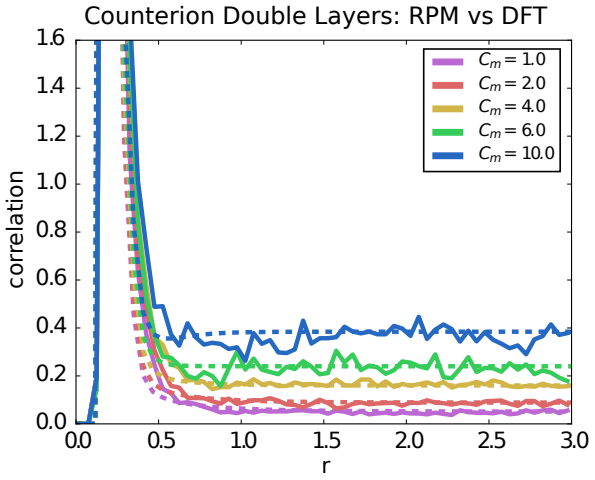

Figure 16: *Comparison of the counterion densities for the cDFT (dashed curves) and the RPM simulations (solid curves) as a function of distance r from analyte particle, for $\sigma = -3$.*

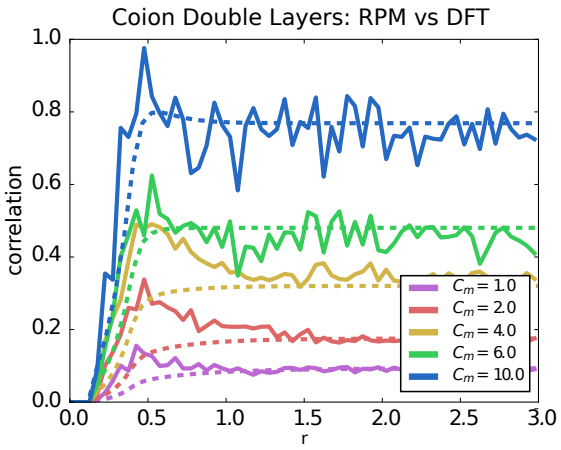

Figure 17: *Comparison of the coion densities for the cDFT (dashed curves) and the RPM simulations (solid curves) as a function of distance r from the analyte particle, for $\sigma = -3$.*

We note that we are using the simplest form of the charge correlation term in the cDFT, namely the MSA expression for the direct correlation function $c(r)$, evaluated at the bulk density of the ions (i.e. the densities in the middle of the channel). In our previous study of the interactions between charged nanoparticles in electrolyte, we found good agreement between cDFT and MD simulations in the density profiles [48]. However, for our cDFT approach and for comparable regimes to our current studies, discrepancies have been previously observed with simulations having large ion concentrations and in regions near to highly charged walls in the work of Oleksy and Hansen [38]. Oleksy and Hansen compared cDFT to Monte Carlo simulations for a 1:1 electrolyte at 1M concentration near a charged wall with reduced charge density $\sigma^* = 0.42$ [38]. They also included a hard sphere solvent, and found differences in the ion density profiles of similar magnitude to those found in our work. Improvements to the charge correlation term, such as using the local weighted density in the calculation of $c(r)$, leads to excellent agreement between cDFT and e.g. molecular dynamics (MD) simulations near highly charged surfaces [31]. The RFD functional

of Gillespie and coworkers [16], which uses a local weighted density in $c(r)$, has been shown to give good agreement with simulation results and experiment in a variety of studies [15, 16]. Thus, in strongly charged regimes a more sophisticated approach beyond the simple bulk MSA treatment is needed to capture ion correlations if quantitative accuracy is sought near surfaces. In this paper, our main focus was to gain further insight into the qualitative role of charge correlations, so the more simple cDFT treatment is adequate. We also note that to our knowledge, more sophisticated treatments of charge correlations have not yet been implemented in a cDFT code that can also do 3D calculations in the geometry we study here.

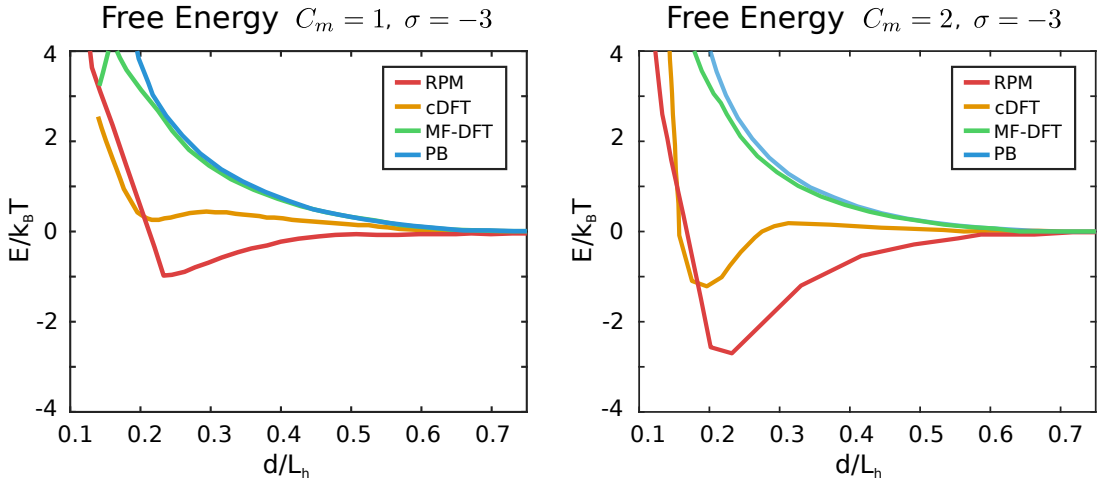

Figure 18: *Comparison of the free energy as a function of particle position in the nanochannel for cDFT, mean-field cDFT, and PB theory with the RPM simulations.*

Next we consider the free energy for the analyte particle as a function of position in the nanochannel. For systems with large ionic concentrations and high charge density on the particle, the cDFT becomes computationally difficult to converge given the localized structures that develop within the density fields. In Figure 18 we compare cDFT to the RPM results only for $\sigma = -3$ and $C_m = 1.0$ and $C_m = 2.0$, values which are accessible with the cDFT computational methods. We see that cDFT captures the trends on a qualitative level compared to the RPM results. In particular, for sufficiently high charge, the cDFT also predicts the development of a free energy minimum for the analyte particle near the wall. In contrast, both the PB theory, which neglects sterics and correlations, and also mean-field cDFT with no charge correlations, are found to predict a purely repulsive interaction energy between the analyte particle and wall. Figure 19 shows cDFT results for differing charge densities on the analyte particle, all at $C_m = 2.0$. As the charge on the particle increases, the depth of the minimum in the free energy increases, as also found (for higher particle charges) by the RPM simulations. In some cases the cDFT also predicts a small barrier in the free energy between the minimum and the center of the channel, but with cDFT we cannot access the high ion concentration regimes where this barrier is as large as in the RPM simulations.

The difficulty in converging the cDFT calculations was surprising, but the systems studied here have higher ion concentrations and surface charge densities than most previous cDFT studies. In

particular, our previous investigation of the interactions between like-charged nanoparticles had maximum ion concentrations of about 220 mM, which is close to the smallest ion concentration in the current study [48]. Decreasing the strength of the electrostatic interactions slightly in the cDFT, by increasing the reduced temperature from $T^* = 0.33$ to $T^* = 0.43$, enabled convergence of systems with higher ion concentration (e.g., the $\sigma = -3$, $C_m = 4$ system). This change corresponds to increasing the ion diameter from 0.232 nm to 3.0 nm. However, further increases would be needed in T^* to get convergence at the higher ion concentrations so we did not pursue those calculations.

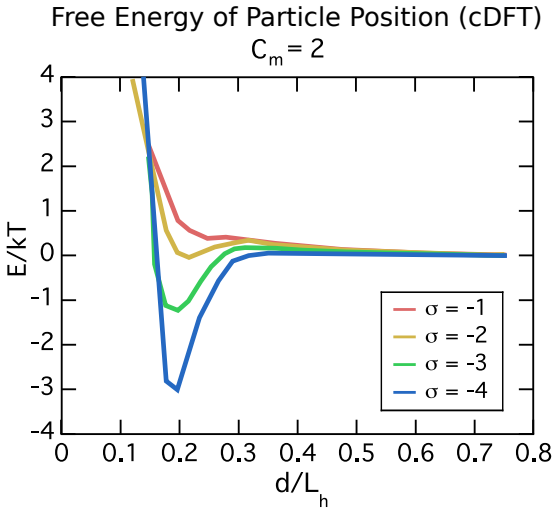

Figure 19: *Free Energy of the Particle Position. Results for classical Density Functional Theory (cDFT) as particle charge σ is varied.*

While cDFT agrees qualitatively with the RPM results there are some significant quantitative discrepancies. The location of the free energy minimum in the cDFT is significantly closer to the nanochannel wall than in the RPM simulations. This is likely due to the somewhat more narrow ion layers in the cDFT. We also find cDFT predicts a depth for the free energy well that is significantly smaller than observed in the RPM results, see Figure 18 and 19. Nevertheless, it is clear from these results that the attractive well results from ion charge correlations.

4. Discussion

In the regimes studied, the ions tend to form clusters in the bulk electrolyte and a compact condensed layer near the channel walls. The interplay between the ionic layers associated with the analyte particle and the wall can result in a significant attraction between the like-charged analyte particle and wall. As discussed in Section 3.1 this occurs at a distance comparable to the thickness of the condensed counterion layer. As can be seen in Figure 3 and 7, there is a secondary layer of negative coions just beyond the counterion layer. At the distance of the free energy minimum, the negatively charged analyte particle joins the secondary layer of negative coions. From our comparisons between the RPM results and the cDFT calculations, we found the attraction to be a consequence of the ion-ion correlations. In contrast the mean-field theories, either PB or mean-field cDFT, that neglect these correlations predict a purely repulsive interaction between the analyte particle and wall.

The free energy of the analyte particle location also exhibits an energy barrier. For the case of the strongly charged analyte particle and ion concentrations ($\sigma = -6$ and $C_m = 8$) there is a significant condensed counterion layer on the particle surface. As the analyte particle approaches the wall, the condensed layer of the analyte particle merges with the condensed wall layer. These rearrangements in some charge regimes result in the free energy barriers as observed in Figure 10. This effect appears to occur only for intermediate ion concentrations of $C_m = 6, 8$, for $\sigma = -3$ and -6, and disappears when the ion concentration becomes sufficiently large. The significant rearrangements that occur as the ion approaches the wall indicate a strong role played by the ion-ion correlations and discrete structures

in determining the free energy of the wall-particle interactions.

It is interesting to consider further the differences between multivalent and monovalent systems. We performed two additional sets of simulations of monovalent systems with 1:1 electrolytes; further details and results are in Appendix B. In the first set of simulations, we keep the number density of the monovalent ions the same as in the multivalent system. While this case results in a different charge density it retains the same entropic contributions in the free energy. In the second we keep the charge density of the system the same but double the number of counterions, which increases the number of charge carriers and the entropic contributions in the free energy. In both cases, we find that the 1:1 electrolyte no longer results in a significant free energy minimum. In the more strongly charged systems with more charge carriers the free energy minimum is further suppressed than in the case of the less charged system which shows a very small (relative to k_BT) and wide region of lower free energy, see Figure 10 and Figure 20. This indicates that the multivalent system may benefit significantly from having less charge carriers which reduce the entropic penalties associated with condensation of charge on the walls and strong correlations at the analyte particle surface. There is also more of an energy gain or less entropic loss when sharing a screening charge in common. It can also be seen in the monovalent systems that the electrolyte is more diffuse, without the presence of transient ion clusters as in the multivalent system. The RPM results indicate that it is the asymmetry between the ion charges and the reduced entropic penality for forming discrete structures that is responsible for the rich phenomena seen in multivalent electrolytes and charged systems.

Thus, the RPM results show that both the ion correlations, and the resulting discrete ion configurations, play important roles in determining the free energy of the system. In the RPM simulations strong electrostatic interactions and multivalent ions can result in the formation of discrete clusters, and the interactions can be mediated at the level of individual ions and their arrangements, as seen in Figures 1, 8 and 11. This is expected to pose significant challenges in formulating constitutive equations for continuum descriptions of the system and in making quantitative predictions. The radial distribution functions we report for the counterions and coions for the bulk and near the wall may be helpful toward that aim, see Figure 12 and 13. The significant quantitative differences between the cDFT and the RPM results arise from the correlation terms in the cDFT functional that are based on the mean-spherical approximation (MSA) for bulk electrolytes. It would be of interest in future work to examine whether the RFD functional [16], which is still based on the MSA direct correlation function but for the local (inhomogeneous) rather than bulk density, would be sufficient to match the present RPM results, or whether improved expressions for the direct correlation function, such as from the new DH-extended MSA (DHEMSA) closure of Olvera de la Cruz and coworkers [62], would give better agreement. However, it may also be the case that for nano systems with finite numbers of ions, finite ion numbers lead to effects that cannot be captured by density functional theories which by construction only include the average ion density.

5. Conclusion

We have investigated in the intermediate coupling regime the behaviors of charged analyte particles when confined within nanochannels. We have found for multivalent 2:1 electrolytes that strong ion-ion correlations can develop that give interesting free energy profiles for the analyte particle position within the channel. We found that the profile can exhibit an energy barrier for intermediate charge regimes and develop a significant energy well in proximity to the channel wall. We found this appears to be related to the over-

charging of the double-layer that forms near the analyte particle surface, see Figure 9. Comparisons between our RPM simulations and cDFT and PB theory indicate the strong role played by ion-ion correlations. The mean-field PB theory, as expected, is inadequate in capturing even the qualitative features of the RPM results. The cDFT approach is found to capture at a qualitative level the main trends seen in the RPM results both for the ionic densities and for the free energy profile as the charge of the system is varied. However, the cDFT results have quantitative discrepancies with the RPM results, in both the ionic layer densities near the walls and in the depth of the free energy well. This arises from the MSA approach used for the charge correlation term, which is based on hard-sphere models of the bulk electrolyte. Our RPM results indicate that near surfaces the ions can form interesting ionic structures such as clusters or discrete layers differring from the bulk and likely requiring further development of correlation terms for cDFT to obtain more quantitative accuracy.

The results we report could have implications for many phenomena within nanochannels and more broadly nanodevices that rely upon electrical effects. For instance, in the case of capillary electrophoresis the free energy profile indicates that analyte particles within the device may hop between states close to the nanochannel wall and close to the channel center. This could significantly affect arrival time observations. More generally, our results show that discrete ion-ion interactions may play a dominate role in nanodevices requiring more sophisticated theory than proivided by traditional mean-field approaches such as the widely used Poisson-Boltzmann theory. Toward this aim in developing better correlation terms for cDFT our bulk and wall radial distribution results may be useful. Many of our results are expected to be useful in gaining insights into other charged systems such as biological macromolecules where similar discrete ion interactions and collective effects may be relevant.

6. Acknowledgments

The authors P.J.A and I.S. acknowledge support from research grant NSF CAREER DMS-0956210, NSF DMS - 1616353, W. M. Keck Foundation, and DOE ASCR CM4 DE-SC0009254. We also acknowledge UCSB Center for Scientific Computing NSF MRSEC (DMR-1121053) and UCSB MRL NSF CNS-0960316. The authors would also like to thank Kai Sikorski for discussions and work developing codes for LAMMPS. This work is supported by the Applied Mathematics Program within the Department of Energy (DOE) Office of Advanced Scientific Computing Research (ASCR) as part of the Collaboratory on Mathematics for Mesoscopic Modeling of Materials (CM4). This work was performed, in part, at the Center for Integrated Nanotechnologies, an Office of Science User Facility operated for the U.S. Department of Energy (DOE) Office of Science. Sandia National Laboratories is a multi-mission laboratory managed and operated by National Technology and Engineering Solutions of Sandia, LLC., a wholly owned subsidiary of Honeywell International, Inc., for the U.S. Department of Energy's National Nuclear Security Administration under contract DE-NA0003525.

References

[1] E Allahyarov, I D'Amico, and H Lowen. Attraction between Like-Charged Macroions by Coulomb Depletion. *Phys Rev Lett*, 81(6):1334–1337, 1998.

[2] Paul J Atzberger and Peter R Kramer. Theoretical framework for microscopic osmotic phenomena. *Phys Rev E Stat Nonlin Soft Matter Phys*, 75(6 Pt 1):061125, Jun 2007.

[3] Nathan A. Baker, David Sept, Simpson Joseph, Michael J. Holst, and J. Andrew McCammon. Electrostatics of nanosystems: Application to microtubules and the ribosome.

Proceedings of the National Academy of Sciences, 98(18):10037–10041, August 2001.

[4] Fabio Baldessari. Electrokinetics in nanochannels: Part I. Electric double layer overlap and channel-to-well equilibrium. *Journal of Colloid and Interface Science*, 325(2):526–538, September 2008.

[5] Martin Z. Bazant. *Induced-Charge Electrokinetic Phenomena*, chapter X, pages 221–297. Springer Vienna, Vienna, 2011.

[6] Victor A. Bloomfield. Condensation of dna by multivalent cations: Considerations on mechanism. *Biopolymers*, 31(13):1471–1481, 1991.

[7] D. Chandler. *Introduction to Modern Statistical Mechanics*. Oxford, New York, 1987.

[8] Siddhartha Das and Suman Chakraborty. Implications of Interactions between Steric Effects and Electrical Double Layer Overlapping Phenomena on Electro-Chemical Transport in Narrow Fluidic Confinements. *arXiv:1010.5731 [cond-mat]*, October 2010. arXiv: 1010.5731.

[9] L. Derjaguin, B.; Landau. Theory of the stability of strongly charged lyophobic sols and of the adhesion of strongly charged particles in solutions of electrolytes. *Acta Physico Chemica URSS*, 633(14), 1941.

[10] R Evans. The nature of the liquid-vapour interface and other topics in the statistical mechanics of non-uniform, classical fluids. *Advances in Physics*, 28(2):143–200, April 1979.

[11] L J D Frink, A G Salinger, M P Sears, J D Weinhold, and A L Frischknecht. Numerical challenges in the application of density functional theory to biology and nanotechnology. *Journal of Physics: Condensed Matter*, 14(46):12167, 2002.

[12] Laura J Douglas Frink, Amalie L Frischknecht, Michael A Heroux, Michael L Parks, and Andrew G Salinger. Toward quantitative coarse-grained models of lipids with fluids density functional theory. *J Chem Theory Comput*, 8(4):1393–1408, 2012.

[13] C. W. Gardiner. *Handbook of stochastic methods*. Series in Synergetics. Springer, 1985.

[14] I. M. Gelfand and S. V. Fomin. *Calculus of Variations*. Dover, 2000.

[15] Dirk Gillespie, Aditya S. Khair, Jaydeep P. Bardhan, and Sumita Pennathur. Efficiently accounting for ion correlations in electrokinetic nanofluidic devices using density functional theory. *Journal of Colloid and Interface Science*, 359(2):520–529, July 2011.

[16] Dirk Gillespie, Mnika Valisk, and Dezso Boda. Density functional theory of the electrical double layer: the RFD functional. *Journal of Physics: Condensed Matter*, 17(42):6609, 2005.

[17] David J. Griffiths. *Introduction to Electrodynamics (3rd Edition)*. Benjamin Cummings, 1998.

[18] Niels Grønbech-Jensen, Keith M Beardmore, and Philip Pincus. Interactions between charged spheres in divalent counterion solution. *Physica A*, 261(1-2):74–81, 1998.

[19] Lin Guo, Shiyi Chen, and Mark O. Robbins. Multi-scale simulation method for electroosmotic flows. *The European Physical Journal Special Topics*, 225(8):1551–1582, 2016.

[20] Jean-Pierre Hansen and Hartmut Lwen. Effective interactions between electric double layers. *Annual Review of Physical Chemistry*, 51(1):209–242, 2000. PMID: 11031281.

[21] Douglas Henderson, Stanisław Lamperski, Zhehui Jin, and J Z Wu. Density Functional Study of the Electric Double Layer Formed by a High Density Electrolyte. *J Phys Chem B*, 115(44):12911–12914, 2011.

[22] Michael A. Heroux, Andrew G. Salinger, and Laura J. D. Frink. Parallel segregated schur complement methods for fluid density functional theories. *SIAM Journal on Scientific Computing*, 29(5):2059–2077, 2007.

[23] Hockney and Eastwood. *Computer Simulation Using Particles,*. Adam Hilger, 1989.

[24] M Kandu, A Naji, Y S Jho, P A Pincus, and R Podgornik. The role of multipoles in counterion-mediated interactions between charged surfaces: strong and weak coupling. *Journal of Physics: Condensed Matter*, 21(42):424103, 2009.

[25] Brian J. Kirby. *Micro-and nanoscale fluid mechanics: transport in microfluidic devices*. Cambridge University Press, 2010.

[26] Brian J. Kirby and Ernest F. Hasselbrink. Zeta potential of microfluidic substrates: 1. Theory, experimental techniques, and effects on separations. *Electrophoresis*, 25(2):187–202, 2004.

[27] Ilya Koltover, Kathrin Wagner, and Cyrus R. Safinya. Dna condensation in two dimensions. *Proceedings of the National Academy of Sciences*, 97(26):14046–14051, 2000.

[28] Michael Kuron and Axel Arnold. Role of geometrical shape in like-charge attraction of dna. *The European Physical Journal E*, 38(3):20–, 2015.

[29] Amy E. Larsen and David G. Grier. Like-charge attractions in metastable colloidal crystallites. *Nature*, 385(6613):230–233, January 1997.

[30] A. W. C. Lau, D. B. Lukatsky, P. Pincus, and S. A. Safran. Charge fluctuations and counterion condensation. *Phys. Rev. E*, 65(5):051502–, April 2002.

[31] Jonathan W. Lee, Robert H Nilson, Jeremy A. Templeton, Stewart K Griffiths, Andy Kung, and Bryan M. Wong. Comparison of Molecular Dynamics with Classical Density Functional and Poisson–Boltzmann Theories of the Electric Double Layer in Nanochannels. *J Chem Theory Comput*, 8(6):2012–2022, 2012.

[32] GA Mansoori, NF Carnahan, KE Starling, and TW Leland. Equilibrium thermodynamic properties of misture of hard spheres. *J Chem Phys*, 54(4):1523–&, 1971.

[33] J. Andrew McCammon and Stephen C. Harvey. *Dynamics of Proteins and Nucleic Acids*. Cambridge University Press, 1987.

[34] A. G. Moreira and R. R. Netz. Strong-coupling theory for counter-ion distributions. *EPL (Europhysics Letters)*, 52(6):705, 2000.

[35] Andre. Moreira and Roland R. Netz. Binding of similarly charged plates with counterions only. *Phys. Rev. Lett.*, 87(7):078301–, July 2001.

[36] Richard P. Muller, Randall T. Cygan, Jie Deng, Amalie L. Frischknecht, John C. Hewson, Michael P. Kanouff, Richard Larson, Harry K. Moffat, Craig M. Tenney, Peter A. Schultz, and Gregory J. Wagner. Modeling thermal abuse in transportation batteries. Technical Report SAND2012-7816, Sandia National Laboratories, Albuquerque, New Mexico and Livermore, California, 2012.

[37] Ekaterina Nagornyak, Hyok Yoo, and Gerald H. Pollack. Mechanism of attraction between like-charged particles in aqueous solution. *Soft Matter*, 5:3850–3857, 2009.

[38] Anna Oleksy and Jean-Pierre Hansen. Towards a microscopic theory of wetting by ionic solutions. I. Surface properties of the semi-primitive model. *Mol Phys*, 104(18):2871–2883, 2006.

[39] Abby L. Parrill and Kenny Lipkowitz. *Reviews in Computational Chemistry, Volume 28, page 226*. Wiley, 2015.

[40] Lus Pegado, Bo Jnsson, and Hkan Wennerstrm. Like-charge attraction in a slit system: pressure components for the primitive model and molecular solvent simulations. *Journal of Physics: Condensed Matter*, 20(49):494235, 2008.

[41] Sumita Pennathur and Juan G. Santiago. Transport Mechanisms in Electrokinetic Nanoscale Channels. *Fluids Engineering Conference*, pages 191–196, January 2004.

[42] Steve Plimpton. Fast parallel algorithms for short-range molecular dynamics. *Journal of Computational Physics*, 117(1):1 – 19, 1995.

[43] E.L. Pollock and Jim Glosli. Comments on p3m, fmm, and the ewald method for large periodic coulombic systems. *Computer Physics Communications*, 95(2):93 – 110, 1996.

[44] Andrei D. Polyanin and Alexander V. Manzhirov. *Handbook of Mathematics for Engineers and Scientists*. Taylor & Francis, 2007.

[45] R Roth, R Evans, A Lang, and G Kahl. Fundamental measure theory for hard-sphere mixtures revisited: the white bear version. *J Phys-Condens Mat*, 14(46):12063–12078, 2002.

[46] W. Ryzsko, A. Patrykiejew, S. Sokoowski, and O. Pizio. Phase behavior of a two-dimensional and confined in slitlike pores square-shoulder, square-well fluid. *The Journal of Chemical Physics*, 132(16):164702, 2010.

[47] John E. Sader and Derek Y.C. Chan. Long-range electrostatic attractions between identically charged particles in confined geometries: An unresolved problem. *Journal of Colloid and Interface Science*, 213(1):268 – 269, 1999.

[48] K. Michael Salerno, Amalie L. Frischknecht, and Mark J. Stevens. Charged nanoparticle attraction in multivalent salt solution: A classical-fluids density functional theory and molecular dynamics study. *J. Phys. Chem. B*, 120(26):5927–5937, July 2016.

[49] H. Schiessel and P. Pincus. Counterion-condensation-induced collapse of highly charged polyelectrolytes. *Macromolecules*, 31(22):7953–7959, 1998.

[50] Todd M. Squires and Stephen R. Quake. Microfluidics: Fluid physics at the nanoliter scale. *Rev. Mod. Phys.*, 77(3):977–, October 2005.

[51] M J Stevens. Simple simulations of dna condensation. *Biophysical Journal*, 80(1):130–139, January 2001.

[52] Hui Sun, Jiayi Wen, Yanxiang Zhao, Bo Li, and J. Andrew McCammon. A self-consistent phase-field approach to implicit solvation of charged molecules with poisson-boltzmann electrostatics. *The Journal of Chemical Physics*, 143(24):243110, 2015.

[53] G.M. Torrie and J.P. Valleau. A monte carlo study of an electrical double layer. *Chemical Physics Letters*, 65(2):343 – 346, 1979.

[54] John P. Valleau and L. Kenneth Cohen. Primitive model electrolytes. i. grand canonical monte carlo computations. *The Journal of Chemical Physics*, 72(11):5935–5941, 1980.

[55] John P. Valleau, L. Kenneth Cohen, and Damon N. Card. Primitive model electrolytes. ii. the symmetrical electrolyte. *The Journal of Chemical Physics*, 72(11):5942–5954, 1980.

[56] J. Th. G. Verwey, E. J. W.; Overbeek. *Theory of the stability of lyophobic colloids*. Amsterdam: Elsevier., 1948.

[57] Qian-Hong Wan. Effect of Electrical Double-Layer Overlap on the Electroosmotic Flow in Packed-Capillary Columns. *Analytical Chemistry*, 69(3):361–363, February 1997.

[58] John D. Weeks, David Chandler, and Hans C. Andersen. Role of repulsive forces in determining the equilibrium structure of simple liquids. *J. Chem. Phys.*, 54(12):5237–5247, June 1971.

[59] Chen-Hung Wu, Thomas G. Fai, Paul J. Atzberger, and Charles S. Peskin. Simulation of osmotic swelling by the stochastic immersed boundary method. *SIAM Journal on Scientific Computing*, 37(4):B660–B688, 2015.

[60] In-Chul Yeh and Max L Berkowitz. Ewald summation for systems with slab geometry. *Journal of Chemical Physics*, 111(7):3155–3162, 1999.

[61] Yang-Xin Yu and J Z Wu. Structures of hard-sphere fluids from a modified fundamental-measure theory. *J Chem Phys*, 117(22):10156–10164, 2002.

[62] Jos W Zwanikken, Prateek K Jha, and Monica Olvera de la Cruz. A practical integral equation for the structure and thermodynamics of hard sphere Coulomb fluids. *J Chem Phys*, 135(6):064106, 2011.

A. Classical Density Functional Theory (cDFT) Formulation

We provide here some additional discussion and details concerning our formulation of the cDFT. As we discussed in Section 2.2, the Helmholtz free energy consists of the terms:

$$\begin{aligned} F\left[\rho_\alpha(\mathbf{r})\right] &= F_{id}\left[\rho_\alpha(\mathbf{r})\right] + F_{hs}\left[\rho_\alpha(\mathbf{r})\right] \\ &+ F_{coul}\left[\rho_\alpha(\mathbf{r})\right] + F_{corr}\left[\rho_\alpha(\mathbf{r})\right]. \end{aligned} \tag{26}$$

The terms represent respectively the Helmholtz free energies for the ideal gas (id), hard spheres (hs), mean-field Coulombic interactions (coul), and second order charge correlations (corr). The term F_{id} is the free energy of an ideal gas which incorporates the translational free energy as

$$\begin{aligned} &F_{id}[\rho_\alpha(\mathbf{r})] \\ &= k_B T \sum_\alpha \int d\mathbf{r} \rho_\alpha(\mathbf{r}) \left[\ln(\Lambda_\alpha^3 \rho_\alpha(\mathbf{r})) - 1\right]. \end{aligned} \tag{27}$$

Here the thermal de Broglie wavelengths Λ_α are constants throughout and do not influence the free energy of the system, so they will be neglected.

For the hard sphere contribution F_{hs} we use the fundamental measure theory of [45, 61] given by

$$F_{hs}\left[\rho_\alpha(\mathbf{r})\right] = k_B T \int d\mathbf{r}\, \Phi[n_\gamma(\mathbf{r})]. \tag{28}$$

The energy density for the hard sphere system Φ is a functional of the Rosenfeld nonlocal (weighted) densities n_γ given by

$$\begin{aligned} \Phi &= -n_0 \ln(1-n_3) \\ &+ \frac{n_1 n_2 - n_{V1}\cdot n_{V2}}{1-n_3} \\ &+ \left(n_2^3 - 3 n_2 n_{V2}\cdot n_{V2}\right)\cdot \\ &\cdot \frac{n_3 + (1-n_3)^2 \ln(1-n_3)}{36\pi n_3^2 (1-n_3)^2}. \end{aligned} \tag{29}$$

The nonlocal densities are

$$n_\gamma(\mathbf{r}) = \sum_\alpha \int d\mathbf{r}'\, \rho_\alpha(\mathbf{r}) \omega_\alpha^{(\gamma)}(\mathbf{r}-\mathbf{r}'), \tag{30}$$

where $\omega_\alpha^{(\gamma)}$ are the weight functions. The weight functions are based on geometric properties of the interactions between hard spheres and are given by the specific forms

$$\begin{aligned} \omega_\alpha^{(2)}(\mathbf{r}) &= \delta(R_\alpha - |\mathbf{r}|), & \omega_\alpha^{(3)}(\mathbf{r}) &= \theta(R_\alpha - |\mathbf{r}|), \\ \omega_\alpha^{(0)}(\mathbf{r}) &= \frac{\omega_\alpha^{(2)}(\mathbf{r})}{4\pi R_\alpha^2}, & \omega_\alpha^{(1)}(\mathbf{r}) &= \frac{\omega_\alpha^{(2)}(\mathbf{r})}{4\pi R_\alpha}, \\ \omega_\alpha^{(V2)}(\mathbf{r}) &= \frac{\mathbf{r}}{r}\delta(R_\alpha - |\mathbf{r}|), & \omega_\alpha^{(V1)}(\mathbf{r}) &= \frac{\omega_\alpha^{(V2)}(\mathbf{r})}{4\pi R_\alpha}. \end{aligned} \tag{31}$$

The $\delta(\mathbf{r})$ denotes the Dirac delta function and the $\theta(\mathbf{r})$ denotes the Heaviside step function. The functional consisting of equation 28 - 31 is designed to match the Mansoori-Carnahan-Starling-Leland (MCSL) equation of state for multi-component hard-sphere fluids [32].

The contribution to the free energy F_{coul} accounts for the mean-field part of the electrostatic interactions as

$$\begin{aligned} &F_{coul}\left[\rho_\alpha(\mathbf{r})\right] \\ &= \frac{1}{2}\sum_{\alpha\beta}\int d\mathbf{r}\int d\mathbf{r}' \rho_\alpha(\mathbf{r})\rho_\beta(\mathbf{r}')\frac{q_\alpha q_\beta}{4\pi\epsilon_0\epsilon|\mathbf{r}-\mathbf{r}'|} \\ &= \frac{1}{2}\sum_\alpha \int d\mathbf{r} q_\alpha \rho_\alpha(\mathbf{r})\phi(\mathbf{r}). \end{aligned} \tag{32}$$

Here q_α is the charge of species α, ϵ_0 is the permittivity of free space, and ϵ denotes the relative dielectric constant. We introduce the electrostatic potential $\phi(\mathbf{r})$ in the second expression.

The contribution to the free energy F_{corr} accounts for the charge correlations of the electrostatic interactions. We use for the charge correlation the approach in [38] with

$$\begin{aligned} &F_{corr}\left[\rho_\alpha(\mathbf{r})\right] \\ &= -\frac{1}{2}k_B T \sum_{\alpha\beta}\int d\mathbf{r}\int d\mathbf{r}' \\ &\qquad \rho_\alpha(\mathbf{r})\rho_\beta(\mathbf{r}')\Delta c_{\alpha\beta}(|\mathbf{r}-\mathbf{r}'|). \end{aligned} \tag{33}$$

The correlation operator is

$$\begin{aligned}\Delta c_{\alpha\beta}(|\mathbf{r}-\mathbf{r}'|) &= c_{\alpha\beta}(r) \\ &+ \frac{q_\alpha q_\beta}{4\pi\epsilon_0\epsilon k_B T|\mathbf{r}-\mathbf{r}'|} \\ &- c^{HS}_{\alpha\beta}(r).\end{aligned} \tag{34}$$

where $c_{\alpha\beta}(r)$ is the direct correlation function for the bulk charged system [38]. The hard sphere and Coulombic terms are subtracted from the full direct correlation function $c_{\alpha\beta}(r)$ in equation 34 to avoid double counting relative to the contributions already in the F_{hs} and F_{coul} terms. The form of $c_{\alpha\beta}(r)$ is taken from the known analytic solution of the mean-spherical-approximation (MSA) for a mixture of charged hard spheres. Detailed expressions can be found in the reference [38].

The grand free energy for the density field of equation 15 is minimized by solving an associated set of Euler-Lagrange equations. This is formulated in terms of residuals with the objective of obtaining densities so that $R_i = 0$. The numerical methods used and other computational details can be found in discussion of the Tramonto package in [11, 12, 22, 36]. The residuals are given by

$$\begin{aligned}R_1 &= \ln\rho_\alpha(\mathbf{r}) + V(\mathbf{r}) - \mu_\alpha \\ &+ \int \sum_\gamma \frac{\partial\Phi}{\partial n_\gamma}(\mathbf{r}')\omega^{(\gamma)}_\alpha(\mathbf{r}-\mathbf{r}')d\mathbf{r}' \\ &+ \sum_\beta \int d\mathbf{r}'\rho_\beta(\mathbf{r}')u_{\alpha\beta}(\mathbf{r}-\mathbf{r}') \\ &- \sum_\beta \int d\mathbf{r}'\rho_\beta(\mathbf{r}')\Delta c_{\alpha\beta}(\mathbf{r}-\mathbf{r}') + Z_\alpha\phi(\mathbf{r})\end{aligned} \tag{35}$$

$$R_2 = n_\gamma(\mathbf{r}) - \sum_\alpha \int d\mathbf{r}'\,\rho_\alpha(\mathbf{r})\omega^{(\gamma)}_\alpha(\mathbf{r}-\mathbf{r}') \tag{36}$$

$$R_3 = \nabla^2\phi - \frac{4\pi}{T^*}\sum_\alpha q_\alpha\rho_\alpha. \tag{37}$$

In these expressions we have adopted the convention that all quantities are in reduced units, so energies are in units of k_BT, lengths in units of d, and valence in terms of Z_α for species α. Additional information concerning classical Density Functional Theory (cDFT) in general can be found in [21, 38] and our specific approach to cDFT in [11, 12, 22, 36].

B. Monovalent Ion Correlations

We performed additional RPM simulations for the nanochannel system with a monovalent 1:1 electrolyte with the conditions that $\sigma = -6$ and $C_m = 2, 8, 10$ and $C_m = 4, 16, 20$. This allows us to make comparisons with the multivalent cases when changing either the total charge of the system or while keeping charge fixed and changing only the number of charge carriers for the counterions. We report the free energy for the analyte particle position for constant number density in Figure 20. We report the ion-ion correlations and radial distribution function $g(r)$ for ions in the bulk and near the wall in Figure 21 and 22. We discuss the $g(r)$ analysis to distinguish these regions in Appendix C.

We find for all of the monovalent cases that there is no significant free energy minimum that forms for a preferred location for the analyte particle within the channel, see Figure 20. This is in contrast to the free energy minima in comparable regimes seen in Figure 10. It is interesting to note that the case with $C_m = 10$ shows some free energy reduction as the analyte particle approaches the wall but it is insignificant relative to k_BT. From observations of the simulation trajectory one can see again significant ion condensation on both the walls and the analyte particle surface. A mechanism similar to that discussed in Section 4 may be at play but it appears the free energy gain is much reduced by the strength of the individual ion charges and entropic penalty associated with monovalent ions.

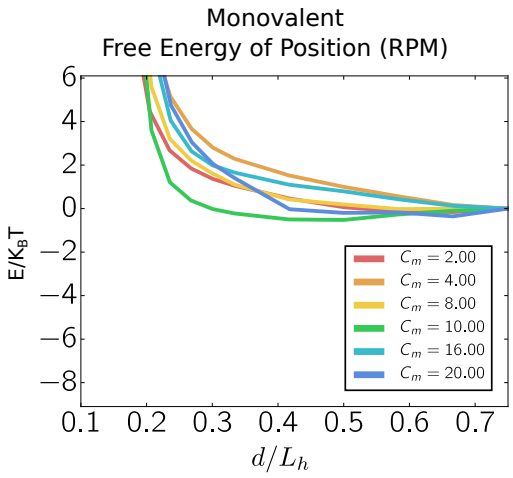

Figure 20: *Free Energy Analyte Particle Position. Monovalent case with* $\sigma = -6$, $C_m = 2, 4, 8, 10, 16, 20$.

We further explore the ion-ion correlations in the monovalent cases. We find that there are correlations between the individual counterions and coions as one may expect. However, in the bulk there is little to no coordination in the counterion-counterion or coion-coion interactions, see Figure 21. Near the walls, while we find there is little to no coordination in the counterion-counterion interactions there is some significant coordination in the coion-coion interactions, see Figure 22. From examination of the simulation trajectory of the system this appears to arise from the transient insertion of coions into the counterion-rich condensed layer near the walls. In contrast to the multivalent case we find for the monovalent electrolyte there are not significant ion clusters or other discrete ion structures that form in the bulk electrolyte.

Finally, cDFT calculations for monovalent electrolyte with $\sigma = -3$ and $C_m = 2, 4$ also show a monotonically increasing free energy as the analyte particle nears the channel wall, in agreement with the RPM results.

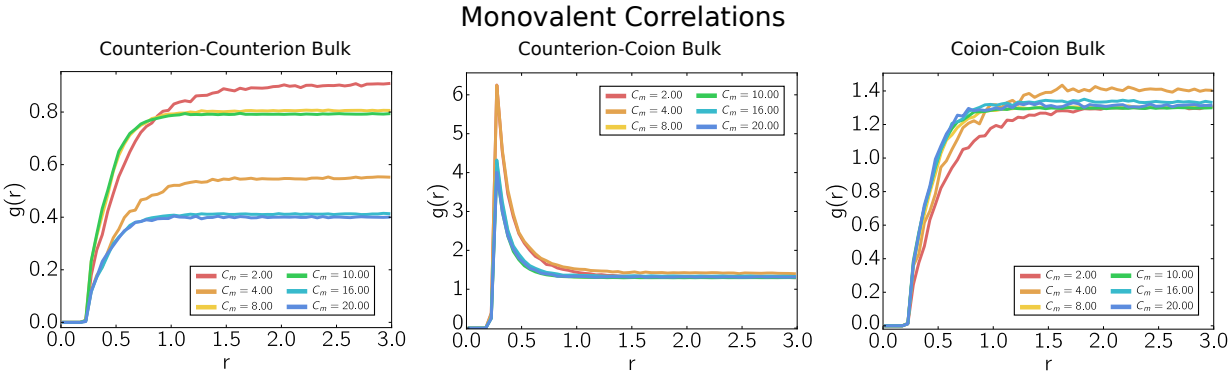

Figure 21: *Ion Correlations in the Bulk. The RDF* $g(r)$ *for ion-ion correlations in proximity to the wall for the monovalent case with* $\sigma = -6$, *and* $C_m = 2, 4, 8, 10, 16, 20$.

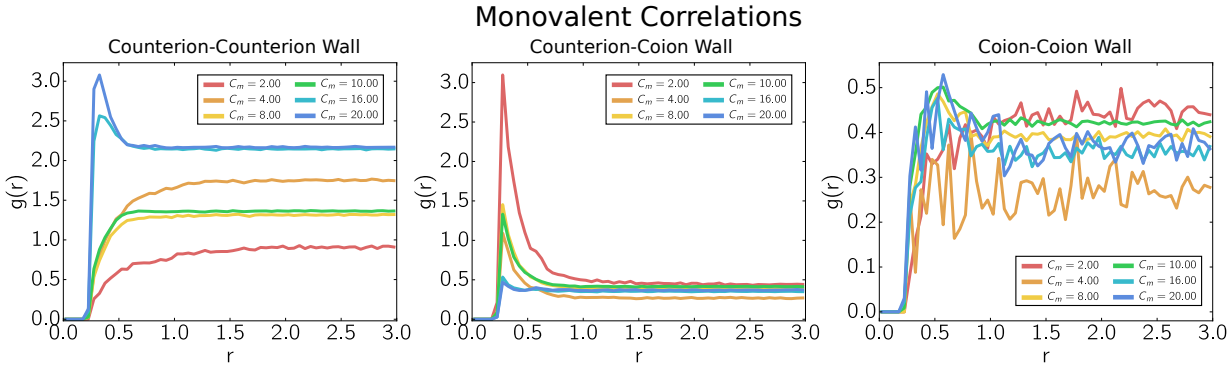

Figure 22: *Ion Correlations near the Wall. The RDF $g(r)$ for ion-ion correlations in proximity to the wall for the monovalent case with $\sigma = -6$, and $C_m = 2, 4, 8, 10, 16, 20$.*

C. Ion-Ion Correlation Analysis

We perform analysis of the radial distribution of the ions taking into account the proxmity of the ions to wall vs the bulk regions and by choosing carefully a normalization taking into account accessible regions of ions. We split the channel into two sampling regions. The first corresponds to the wall case when the base ion is within the distance $d < 1$nm from the channel wall. The second is the bulk case when the base ion is a distance $d > 1$nm from the channel wall. In the confined channel geometry there are limited regions where ions are permitted given either the excluded volume of the wall or intrusion into the bulk or wall sampling region. We handle this by a careful normalization by accessible volume to obtain a radial distribution function $g(r)$. We give details below with a schematic of our approach in Figure 23.

For a bulk system the radial distribution function can be sampled for a base ion by counting the number of ions within a spherical shell at radius r_k and thickness δr to obtain the normalized distribution function $\bar{g}(r_k) = H_k/V_k C_0$. The $V_k = \frac{4\pi}{3}\left(R_k^3 - r_k^3\right)$ is the volume of the spherical shell of thickness δr, $R_k = r_k + \delta r$, H_k is the histogram corresponding to the number of ions within the k^{th} spherical shell, and C_0 is a normalizing constant typically chosen to correspond to the bulk concentration.

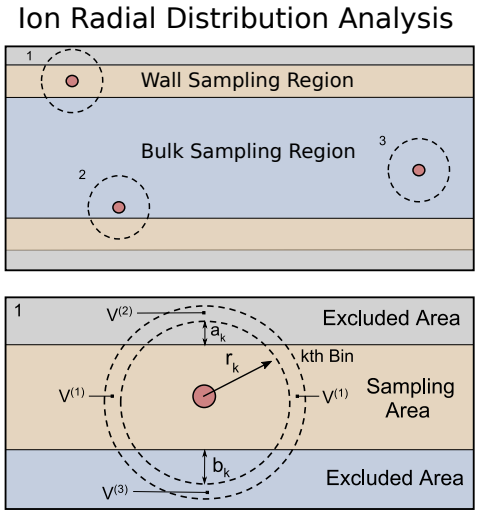

Figure 23: *Ion Radial Distribution Analysis. To distinguish between the behaviors of the ions in the bulk vs near the channel wall in the condensed layer we perform regional sampling of a radial distribution function. To avoid issues with ions excluded from the wall domain or within other sampling region we perform our radial distribution analysis $g(r)$ with probability conditioning on being within permissible regions. We normalize the distribution at a given radius by the accessible volume $V^{(1)}$ of the ions which correspond to spherical caps.*

To obtain a more spatially refined description of the ions taking into account excluded regions we define the radial distribution func-

tion as $g(r_k) = \tilde{H}_k/\tilde{V}_k\tilde{C}_0$ where $\tilde{H}_k$ for a given base ion is the histogram count for all permissible ions in the sampling region within the spherical shell of radius r_k and thickness δr and $\tilde{C}_0$ is a normalization based on the total concentration of ions. To obtain a radial density we use the volume $\tilde{V}_k$ corresponding only to the part of the spherical shell that is within the permissible sampling region. This can be computed using the geometry of spherical caps to obtain $\tilde{V}_k = V^{(1)} = V_k - V^{(2)} - V^{(3)}$ where $V^{(2)} = \frac{\pi}{3}\left(A_k^2\left(3R_k - A_k\right) - a_k^2\left(3r_k - a_k\right)\right)$ and $V^{(3)} = \frac{\pi}{3}\left(B_k^2\left(3R_k - B_k\right) - b_k^2\left(3r_k - b_k\right)\right)$ are the volumes associated with the shell of a spherical cap of thickness δr [44]. We denote by $A_k = a_k + \delta r$, $B_k = b_k + \delta r$, $R_k = r + \delta r$, see Figure 23.

Our radial distribution function can be thought of as the conditional probability function for a pair of ions occupying the sample sampling region. Alternative methods have been considered in the literature such as sorting ions into z-slabs and sampling only in the xy-directions [39, 46]. Both approaches provide very similar information and allow for distinguishing between the behaviors of ions in the bulk region and behaviors of ions in the condensed layer near to the walls.

The approach we have introduced here allows for a unified observable that can transition from calculations involving sampling regions that are relatively narrow similar to z-slabs to intermediate and larger regions that yield results approaching the bulk radial distribution. By use of this radial distribution function, we are able to obtain a refined understanding of how the ion correlations change when in regions in the bulk of the nanochannel versus when an ion occupies the condensed ion layer near to the wall which exhibits a quasi-two dimensional behavior.